Storm time distributions of diffuse auroral electron energy and X-ray flux: Comparison of drift-loss simulations with observations

Margaret W. Chen,[1] Michael Schulz,[2] Phillip C. Anderson,[1,3] Gang Lu,[4] G. Germany,[5] and Martin Wüest[6,7]

Received 6 August 2004; revised 18 November 2004; accepted 21 December 2004; published 15 March 2005.

[1] We investigate the spatial structure of the electron diffuse aurora during the 19 October 1998 storm by comparing drift-loss simulations with precipitating particle data and auroral images. Distributions of precipitating diffuse aurora during magnetic storms depend on variation of the magnetotail electron distributions, electron transport, and electron pitch-angle scattering. In our simulations we compute the bounce-averaged drift motion and precipitation of plasma sheet electrons in Dungey's model magnetosphere (dipole plus uniform southward B_z). We use the Assimilative Model of Ionospheric Electrodynamics (AMIE) electric field. We evaluate the precipitating energy flux and X-ray energy at ionospheric altitude $h = 127.4$ km for two different scattering rate models: (1) strong diffusion everywhere and (2) an MLT-dependent model scattering rate less than everywhere strong. We compare the simulated distributions of electron energy flux with those obtained from *Dst*-binned averaged NOAA-12 data and the Polar/Ultraviolet Imager (UVI). The simulated distributions of X-ray flux are compared with Polar/Polar Ionospheric X-ray Imaging Experiment (PIXIE) images. The comparisons reveal that pitch-angle scattering clearly plays a crucial role in determining the spatial distribution of the precipitating electron energy flux. The simulated storm time energy flux with strong diffusion tends to be much more intense in the evening sector and much weaker near dawn than what is statistically observed. The most intense electron precipitation under strong diffusion will occur where the electron drift times from the plasma sheet are on the order of the electron lifetime against strong diffusion. On the other hand, the model and data comparison shows that MLT-dependent scattering less than everywhere strong produces a more realistic electron diffuse aurora than with strong diffusion. Our study strongly suggests that wave scattering is weak in the postdusk sector (~2200 MLT) and strong in the morning sector (~0400 MLT), which seems to be in general agreement with statistical and storm time wave observations.

Citation: Chen, M. W., M. Schulz, P. C. Anderson, G. Lu, G. Germany, and M. Wüest (2005), Storm time distributions of diffuse auroral electron energy and X-ray flux: Comparison of drift-loss simulations with observations, *J. Geophys. Res.*, *110*, A03210, doi:10.1029/2004JA010725.

1. Introduction

[2] This is a storm time study of diffuse auroral electrons and the auroral X rays they produce. The distributions of precipitating electrons and derived quantities such as total electron energy flux during magnetic storms depend on variations of the source distributions (i.e., magnetotail electron fluxes), electron drift, and electron pitch-angle scattering. In this work we simulate the bounce-averaged drifts and postulate the loss rates of plasma sheet electrons so as to model the storm time electron diffuse aurora. In our past work [*Schulz and Chen*, 1999; *Chen and Schulz*, 2001a, 2001b] we have followed the drift paths of plasma sheet electrons in a simplified convection electric field model that included corotation, a time-independent shielded [*Volland*, 1973, 1975; *Stern*, 1974, 1975] term, and a variable unshielded [*Nishida*, 1966; *Brice*, 1967] term. However, CRRES and DMSP satellite measurements [*Wygant et al.*, 1998; *Rowland and Wygant*, 1998; *Anderson et al.*, 2001], along with Millstone Hill radar measurements [*Yeh et al.*, 1991], show that storm time magnetospheric electric fields are significantly more complicated in spatial structure than the above-mentioned models. In the present study, we use the Assimilative Model of Ionospheric Electrodynamics (AMIE) [*Richmond and Kamide*, 1988], which

[1]Space Sciences Applications Laboratory, The Aerospace Corporation, El Segundo, California, USA.
[2]Lockheed Martin Advanced Technology Center, Palo Alto, California, USA.
[3]Now at University of Texas at Dallas, Richardson, Texas, USA.
[4]High Altitude Observatory, Boulder, Colorado, USA.
[5]University of Alabama, Huntsville, Alabama, USA.
[6]Southwest Research Institute, San Antonio, Texas, USA.
[7]Now at Inficon AG, Balzers, Principality of Liechtenstein.

0148-0227/05/2004JA010725$09.00

features large storm time electric fields in localized regions of MLT at $L \sim 2.5-5$ in the inner magnetosphere. This model allows us to investigate the plasma sheet electron transport more realistically than do the simplified models we have used previously. In this work we consider two electron pitch-angle scattering-rate models: (1) strong pitch-angle diffusion, and (2) a diffusion rate that is less than everywhere strong but dependent on magnetic local time (MLT). Model 1 is a limiting idealization that is useful for comparison with more realistic scattering models.

[3] We apply our scattering without clearly identifying the scattering mechanism that causes diffuse auroral electrons to precipitate. Two main mechanisms for this have been proposed.

[4] Early on, it was believed that electrostatic cyclotron harmonic (ECH) waves (also known as "$n + 1/2$" waves) generated by a loss cone instability would scatter plasma sheet electrons sufficiently to account for the diffuse aurora [*Kennel et al.*, 1970; *Kennel and Ashour-Abdalla*, 1982; *Ashour-Abdalla and Kennel*, 1978]. Early measurements of ECH waves seemed to show sufficient power to scatter 1–20 keV electrons into the auroral loss cone at the required rate [*Scarf et al.*, 1973] if assumed to extend along entire field lines of interest. However, later wave observations at geosynchronous orbit [*Belmont et al.*, 1983], at 4–12 R_E [*Roeder and Koons*, 1989], and at 5–8 R_E [*Koons and Roeder*, 1990] have shown that ECH waves are localized near the equator and do not have enough power to scatter 1–20 keV electrons strongly (i.e., so as to cause pitch-angle isotropy). *Horne and Thorne* [2000] calculated bounce-averaged pitch-angle diffusion rates for ECH waves and similarly concluded that ECH waves do not have enough power to scatter 1–20 keV electrons strongly. At the time, the lack of sufficient ECH power to generate strong diffusion seemed to refute pitch-angle scattering by ECH waves as a viable mechanism for producing the diffuse aurora. However, our recent simulations [*Chen and Schulz*, 2001b] have shown that if strong diffusion occurred over a substantial portion of the plasma sheet electron's drift path, then most of the electrons in a flux tube would precipitate before reaching dawn, leaving too few electrons to account for the brightness of the diffuse aurora observed there. Thus there is not necessarily a requirement for strong diffusion by waves to account for the diffuse aurora.

[5] The other wave mode widely invoked for scattering diffuse auroral electrons is the whistler mode [e.g., *Cornilleau-Wehrlin et al.*, 1985; *Johnstone et al.*, 1993; *Villalón and Burke*, 1995; *Johnstone*, 1996]. *Johnstone et al.* [1993] attributed certain features in the CRRES electron data to whistler-mode interactions and argued in particular that significant low-energy electron precipitation at high latitudes can be accounted for by such interactions. From the shape of electron pitch-angle distributions observed by CRRES, *Meredith et al.* [1999] recently inferred that both whistler-mode (at $L \gtrsim 6$) and ECH waves ($L \lesssim 6$) play significant roles in scattering plasma sheet electrons. More recently, *Horne et al.* [2003] have analyzed whistler mode hiss, chorus, and ECH waves, together with electron pitch-angle distributions measured by CRRES during a small substorm injection. They thereby found that ECH waves probably provided the major contribution to diffuse auroral precipitation for the event studied.

[6] This study focuses on comparing simulations and observations of diffuse auroral precipitation for a particular magnetic storm. While we do not specifically identify the electron scattering mechanisms here, through comparisons of modeled and measured distributions of precipitating electrons we do gain a better understanding of the global transport and scattering of the plasma sheet electrons necessary to produce the observed storm time diffuse aurora. We have chosen the 19 October 1998 storm (minimum $Dst = -112$ nT), partly because this storm has been selected for detailed study by the NSF Geospace Environment Modeling (GEM) Inner Magnetosphere Storms Campaign. Moreover, *Anderson et al.* [2000a, 2000b] analyzed Polar/Polar Ionospheric X-ray Imaging Experiment (PIXIE) and Polar/Ultraviolet Imager (UVI) images in detail for this storm. We will also compare our simulated patterns of precipitating electron energy flux with *Dst*-binned NOAA-12 electron data, averaged over a 10-year interval [*Wüest et al.*, 2005].

2. Simulation Method

[7] We model the magnetospheric **B** field as the superposition of a dipolar magnetic field and a uniform southward $\Delta\mathbf{B}$ parallel to the dipole axis [*Dungey*, 1963]. For this study we have kept $\Delta\mathbf{B}$ constant and have chosen $\Delta\mathbf{B}$(=14.7 nT) in time so that the circular boundary between closed and open field lines intersects the Earth at a constant colatitude $\theta^* = 20°$, and thus the radius of the neutral line is constant during the storm. This leads to a circular neutral line of radius $b = 12.82\ R_E$ in the equatorial plane. This simple field model preserves essential features of the relevant physical processes, while still letting us represent the results of needed subsidiary calculations in terms of analytic functions. The equation of a field line in this model is

$$r = La\left[1 + (1/2)(r/b)^3\right] \sin^2\theta, \tag{1}$$

where r is the geocentric distance, θ is the magnetic colatitude, a is the Earth's radius, and L is the dimensionless magnetic-shell label inversely proportional to the amount of magnetic flux enclosed. The label $L^* = 2b/3a$ of the last closed field line is $L^* = 8.5466$ for $\theta^* = 20°$. In future studies we plan to use a time-varying $\Delta\mathbf{B}$ so that the size of our model magnetosphere varies more realistically during the course of a storm. Such a magnetic field would lead to induced electric fields that we do not consider in the present study.

2.1. Kinematics

[8] To simplify the kinematics underlying this study, we treat the drift of plasma sheet electrons of interest as if they were in strong pitch-angle diffusion. Under strong pitch-angle diffusion the pitch-angle distributions would be essentially isotropic at each electron energy of interest. In the limit of strong scattering, all electrons of a given energy in a given magnetic flux tube would drift together as one under the influence of gradient-B, curvature, and electric forces. The phase-space volume

$$\Lambda \equiv p^3\Psi \equiv p^3 \oint (ds/B), \tag{2}$$

defined by the product of the momentum-space volume that the electrons surround ($4\pi p^3/3$) and the flux-tube volume Ψ that they occupy, is adiabatically invariant in the limit of strong pitch-angle diffusion, even as the usual first and second invariants M and J are strongly violated. It can be shown [*Rosenbluth and Longmire*, 1957; *Southwood*, 1977] that conservation of Λ is analogous to the adiabatic gas law. With conservation of Λ it is implicitly assumed that there is no energy diffusion due to wave-particle interactions. An adiabatically invariant quantity proportionally to $\Lambda^{2/3}$ for nonrelativistic particles is held constant in the Rice Convection Model (RCM) [*Harel et al.*, 1981; *Wolf et al.*, 1982].

[9] Observed particle distributions in the plasma sheet are indeed approximately isotropic by some accounts [e.g., *Stiles et al.*, 1978], but we have found [*Chen and Schulz*, 2001a, 2001b] that truly strong pitch-angle diffusion would cause a diffuse aurora that is more intense than typically observed. In the present study we nevertheless treat particles as if they were in strong pitch angle diffusion so as to simplify our drift calculations, but we employ models with appropriately reduced scattering rates to describe the resulting electron precipitation and loss. We believe this is a reasonable compromise for now. However, we plan to improve upon this treatment of drifts in future work by using eigenmodes of the pitch-angle diffusion operator [*Roberts*, 1969; *Schulz*, 1991, pp. 229–231] as quasi-particles to achieve a smooth transition from isotropy in the plasma sheet to progressively greater anisotropy at lower L values.

[10] In Dungey's model magnetosphere the flux-tube volume Ψ is very well approximated [*Schulz*, 1998] by an analytical expression that depends on L. Thus the Hamiltonian function can be expressed analytically in terms of L. Adiabatic drift shells are surfaces of constant Λ and H if the Hamiltonian function

$$H(L,\phi,t) = \left[(\Lambda/\Psi)^{2/3}c^2 + m_0^2c^4\right]^{1/2} - m_0c^2 + q[-(V_\Omega/L) + \Phi_E(L,\phi,t)] \tag{3}$$

is either time-independent or regarded as being "frozen in time" [e.g., *Chen et al.*, 2003]. Here q is the particle charge, φ is magnetic local time, $-V_\Omega/L$ is the corotation potential (V_Ω = 90 kV), and Φ_E is the electrostatic potential function. We have used (2) to express the momentum in terms of Λ and the flux tube volume.

2.2. Dynamics

[11] In this study we use AMIE, the Assimilative Model of Ionospheric Electrodynamics [*Richmond and Kamide*, 1988], to prescribe the electric potentials in our simulation model. Although commonly displayed as plots, AMIE potentials are in fact based on an analytical expansion in terms of colatitude θ and magnetic local time φ in the ionosphere so that

$$\Phi_{\mathrm{AMIE}}(\theta,\phi,t) = \sum_i a_i(t)\,\Phi_i(\theta,\phi), \tag{4}$$

where the a_i are AMIE expansion coefficients and t denotes time. The scalar basis functions Φ_i are constructed from associated Legendre functions with nonintegral degree n at latitudes 40° and 50° and from trignometric functions at lower latitudes [*Richmond and Kamide*, 1988]:

$$\Phi_i(\theta,\phi) = K_{1i}P_n^{|m|}(\cos\theta)f_m(\phi) \qquad \theta < \theta_0,\ \theta > \pi - \theta_0 \tag{5a}$$

$$= K_{2i}[\cot^m(\theta/2) + \tan^m(\theta/2)]f_m(\phi) \qquad \theta_0 < \theta < \pi - \theta_0 \tag{5b}$$

with

$$f_m(\phi) = \sqrt{2}\cos m\phi \qquad m < 0$$
$$= 1 \qquad m = 0 \tag{6}$$
$$= \sqrt{2}\sin m\phi \qquad m > 0.$$

where $i = (n, m)$, θ_0 is the colatitude (typically chosen to be 40°) at which (5a) and (5b) are forced to match smoothly; m is the azimuthal "wave" number; while K_{1i} and K_{2i} are normalizing constants chosen so that the vector basis functions $\nabla\Phi_i$ are orthonormal over the ionosphere and continuous at $\theta = \theta_0$. The eigenvalues n are determined by matching logarithmic derivatives $\partial\ln\Phi_i(\theta, \varphi)/\partial\theta$, as specified by (5a) and (5b) at $\theta = \theta_0$. AMIE potentials are not usually calculated equatorward of $\theta = \theta_0$ in practice. The AMIE coefficients a_i are determined via least-squares fit of the analytical expansion (4) to magnetometer data and to any available satellite and radar data. AMIE potentials can be mapped analytically to anywhere in the magnetic field model that we use via (1), the equation of the field-line label. According to (1), the relationship between L and θ at the usual altitude $r - a$ = 110 km of the AMIE model is

$$L = 1.017/\sin^2\theta. \tag{7}$$

This relationship allows AMIE potentials to be expressed as $\Phi_{\mathrm{AMIE}}(L, \varphi, t)$, a function of L, φ, and t. More complicated magnetic field models would require a numerical mapping of AMIE potentials [cf. *Boonsiriseth et al.*, 2001]. Further details on the mapping of the AMIE electric field to our field model are included in the work of *Chen et al.* [2003].

[12] For this study we have chosen to simulate the diffuse aurora during the main phase of the 19 October 1998 storm (minimum $Dst = -112$ nT) by using the AMIE electric field corresponding to this storm. Figure 1 shows traces of the Dst index, total AMIE cross-polar-cap potential ($\Delta\Phi$), and components (B_x, B_y, B_z) of the interplanetary magnetic field measured by the IMP, WIND, and ACE satellites during 18–21 October 1998. Figure 1e shows that during the main phase of this storm B_z did not vary widely (only between ~ -11 nT and -18 nT). The dashed vertical lines in Figure 1 correspond to selected times of interest (0800 UT, 0950 UT, 1030 UT, and 1100 UT) during the main phase. Figure 2 shows the equatorial AMIE electric field intensity $|\mathbf{E}|$, evaluated in the Earth's corotating frame, at these times of interest. Figure 2 thus illustrates the spatial and temporal variability of the AMIE electric field during the storm main phase. At 0800 UT the AMIE electric field intensity was

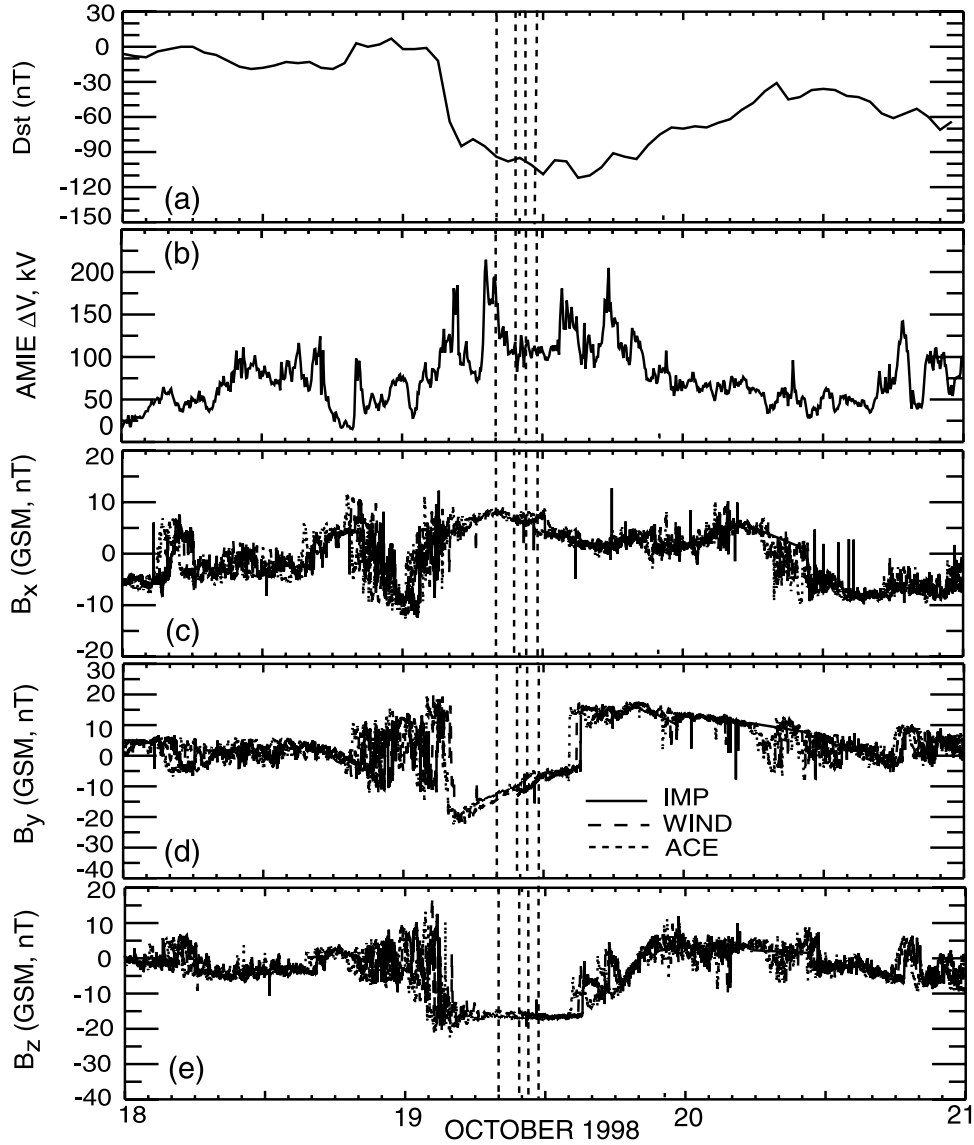

Figure 1. The time traces of (a) the total AMIE cross polar cap potential drop, (b) the *Dst* index, and the GSM (c) x-, (d) y-, and (e) z-components of the interplanetary magnetic field. The location of the satellites in GSE coordinates were ACE (230, −38, −6) R_E, WIND (95, 33, 6) R_E, and IMP (20, −23, −25) R_E. The dashed vertical lines correspond to 0800 UT, 0950 UT, 1030 UT, and 1130 UT on 19 October 1998.

quite strong (>2 mV/m) near dusk at $L \sim 3-7$, as well as in the evening sector at $L \gtrsim 4$ and in the morning sector at $L \sim 3-6$. Electric fields with intensity >2 mV/m spanned regions of narrower radial extent (but still significant) at later times of interest (at 0950 UT, 1030 UT, and 1130 UT).

[13] In Figure 3, we plot contours of constant electron Hamiltonian (or total energy) per unit charge (units of keV) at 0800 UT on 19 October 1998. We considered that the electric field was frozen in time. The dotted circles at b = 12.82 R_E in the equatorial plane (upper panels) correspond to the neutral line and thus to the outer boundary of our model. The contours of constant Hamiltonian correspond to quasi-steady state electron drift paths. Figure 3a shows such contours for $\Lambda = \Lambda_4$ (the value of Λ for corresponding to kinetic energy E = 4 keV at r_0 = 6 R_E) for the AMIE electric field at 0800 UT on 19 October 1998. The plus signs mark 10-min intervals as electrons would drift from the nightside neutral line. For comparison, Figure 3b shows quasi-steady drift paths based on a simplified convection electric field model that we had been using in the past [*Chen and Schulz*, 2001a, 2001b]. This simplified convection model, to which the corotation potential must be added as in (3), was based on an electrostatic potential function

$$\Phi_{simp}(L,\phi) = \frac{V_0}{2}\left(\frac{L}{L*}\right)^2 \sin\phi + \frac{\Delta V(t)}{2}\left(\frac{L}{L*}\right)\sin\phi. \quad (8)$$

The first term of (8) corresponds to a shielded time-independent electric field [*Volland*, 1973, 1975; *Stern*, 1974, 1975] with V_0 = 25 kV; the second term corresponds to a time-variable unshielded electric field [*Nishida*, 1966; *Brice*, 1967]. The quasi drift paths in Figure 3b are

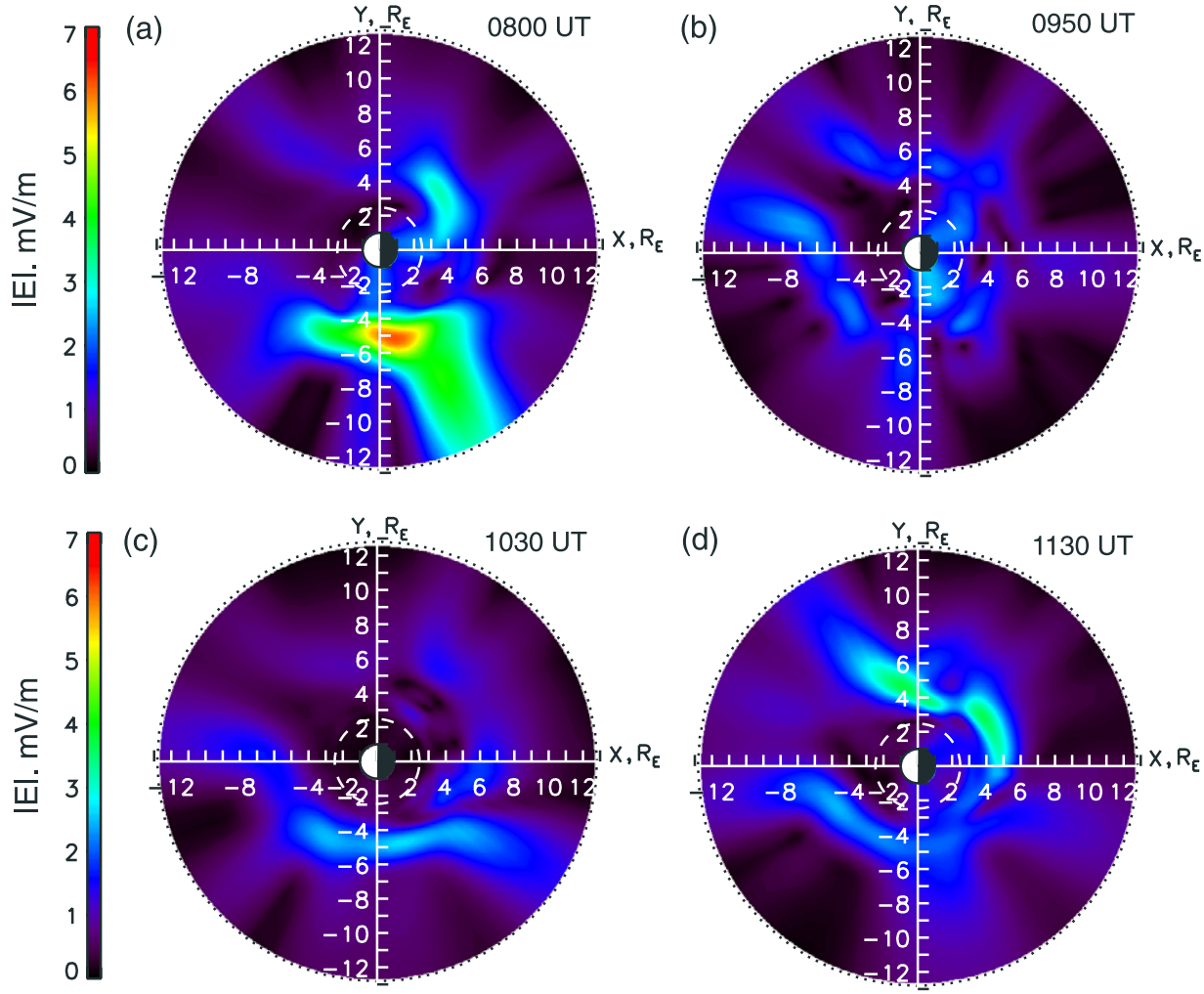

Figure 2. The equatorial electric field intensity |E| in mV/m in the Earth's corotating frame for (a) 000 UT, (b) 0950 UT, (c) 1030 UT, and (d) 1130 UT on 19 October 1998. The white dashed curve at 2.54 R_E maps to the AMIE transitional latitude of 50° in our magnetic field model.

calculated for $\Delta V = 150.5$ kV so as to match the total cross-polar-cap potential ($V_0 + \Delta V = 175.5$ kV) in the AMIE model at 0800 UT on 19 October 1998. Unlike the quasi drift paths in the simplified electric model (Figure 3b), the AMIE quasi-steady drift paths (Figure 3a) are not symmetric between day and night. The extra strength of the AMIE electric field in the evening sector leads to larger drift rates there and leads to rapid access of electrons from the nightside neutral line to $R_0 \approx 4$ near dusk for electrons with energies of 0 to 64 keV at $R_0 = 6$. Examples of equatorial AMIE quasi-steady drift paths for electrons with energies of 0, 5, 13, and 38 keV at $R_0 = 6$ for 0800 UT on 19 October 1998 were shown in Figure 9 of *Chen et al.* [2003]. Those quasi-drift paths corresponded to electrons that conserved their first two invariants rather than Λ, but they qualitatively illustrated the same quasi-drift topology as is seen in Figure 3a here for a wide range of plasma sheet electron energies. More generally, *Chen et al.* [2003] found that during storm main phases the AMIE electric equipotentials tend to be concentrated in some narrow sector of MLT on the nightside so as to yield rapid inward transport of particles from the nightside neutral line to low L values in that sector.

[14] To illustrate the significance of these quasi-drift paths for the diffuse aurora, we map them by means of (1) to an altitude $h = 0.02\ R_E = 127.4$ km in the auroral ionosphere. Figures 3c and 3d show such mappings of the drift paths for $\Lambda = \Lambda_4$ (subscripts on Λ denote the corresponding kinetic energy in keV at $r_0 = 6\ R_E$) shown in Figures 3a and 3b, respectively. In our polar region plots the azimuthal coordinate φ still represents magnetic local time (MLT), but the "radial" coordinate is the value of $\sin\theta$ at $r = a + h = 1.02\ R_E$. The dotted circles here correspond to values of $\sin\theta_h$ at latitudes of 80°, 70°, 60°, and 50°. All polar region plots shown in this paper have this same format and correspond to an altitude of 127.4 km. From Figures 3c and 3d, one can see how the representative quasi-drift paths from the plasma sheet would map equatorward of the polar cap, which is bounded by a fixed circle at 70° latitude on the Earth (69.8° at $r = a + h$) in our specification of Dungey's model magnetosphere. Figure 3c shows that the plasma sheet electrons could reach latitudes as low as ~52° in the evening sector where the AMIE electric field is strongest at 0800 UT on 19 October 1998, if the AMIE electric field were constant in time. Figure 3d shows that plasma sheet electrons in the simplified electric field model (with the

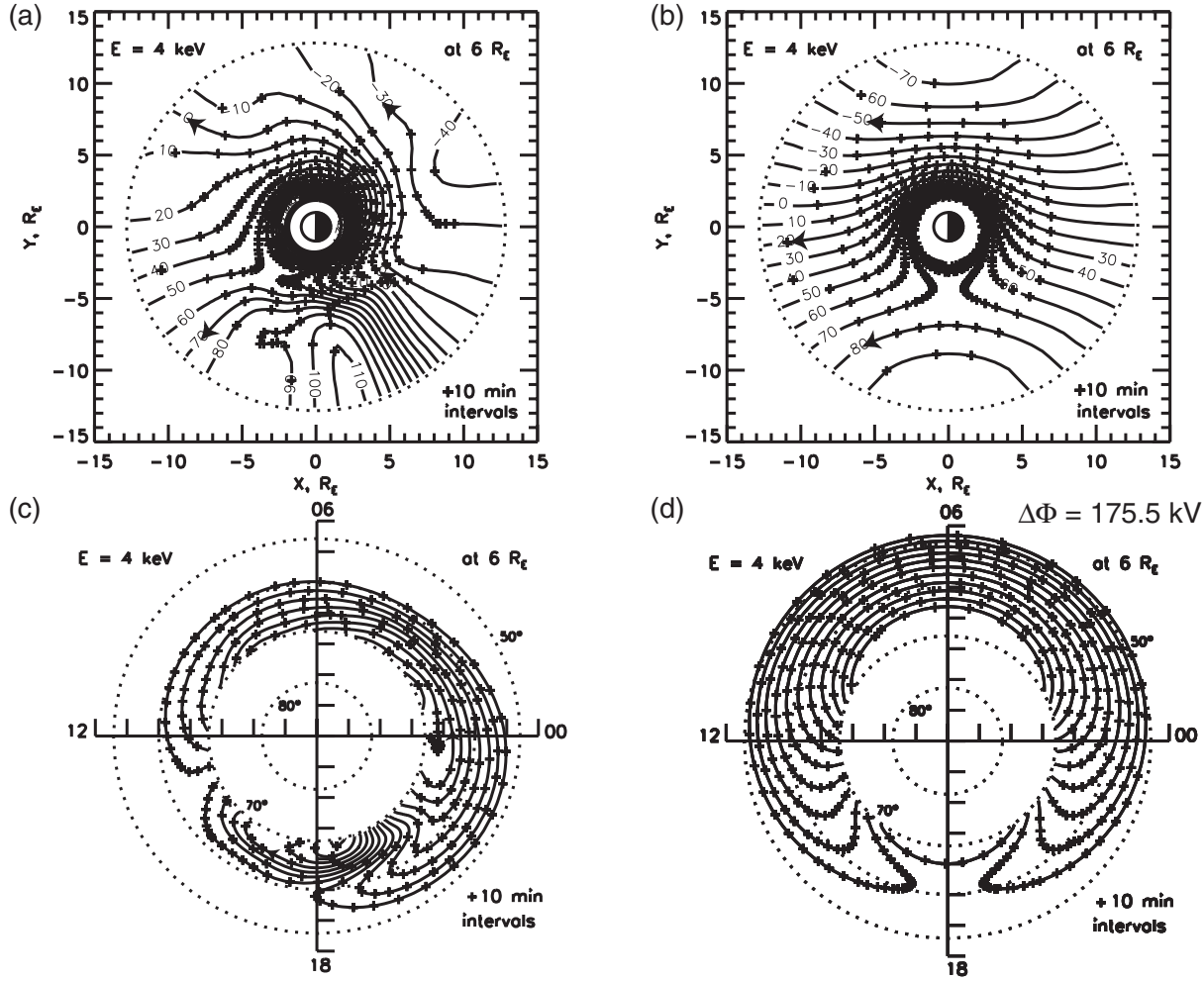

Figure 3. Equatorial intercepts and polar projections of drift shells of electrons with $\Lambda = \Lambda_4$ (4 keV at 6 R_E) in a snapshot of (a), (c) the AMIE electric field model for 0800 UT on 19 October 1998 and (b), (d) the simplified electric field model for the cross polar cap potential of 175.5 kV, same total AMIE cross polar cap potential drop at 0800 UT on 19 October 1998.

same total cross polar cap potential drop here as in the AMIE model) reach the lowest latitudes (~49°) at dawn.

[15] Quasi-steady drift paths are useful for illustrating the drift topology. However, for our actual simulations we calculate drift caused by a time-varying AMIE electric field. We linearly interpolate between 5-min AMIE coefficients to obtain the time-dependent coefficients $a_j(t)$ in (4). Bounce-averaged drift rates for electrons in strong pitch-angle diffusion are easily derived from the Hamiltonian function [see *Schulz*, 1998]. We solve the drift equations numerically by using the Bulirsch-Stoer extrapolation method [e.g., *Press et al.*, 1986, pp. 563–569]. Here we perform these simulations for eight Λ values (corresponding to energies 0.25, 0.5, 1, 2, 4, 8, 32, and 64 keV at $R_0 = 6$, which corresponds to $L \approx 5.707$ in our model) and interpolate as necessary. In the field model that we use here, an equatorial radial distance of $R_0 = 6$ maps to 65° latitude at $r = a + h = 1.02\ R_E$. For each Λ value of interest we set up a grid of about 2000–3000 points spaced every 5° in longitude and every 0.01 in $\sin\theta_h$. We start our representative electrons on the magnetic field lines corresponding to these grid points and then run the simulation backward in time, thereby tracing the trajectories back to where and when the electrons would have been very close to the boundary of our model ($L \approx 8.5$).

[16] It is instructive to compute the transport time Δt required for a plasma sheet electron to drift from the boundary of our model (i.e., from the neutral line) to any field line of interest. The transport times Δt for electrons having $\Lambda = \Lambda_4$ during the main phase of the 19 October 1998 storm are shown in Figures 4a (0800 UT), 4b (0950 UT), 4c (1030 UT), and 4d (1130 UT). The color scale indicates the drift time required for an electron to have reached the indicated latitude and longitude at $r = a + h$ at each of the four times of interest. In these examples, the transport times to 60° latitude ($R_0 = 4.2$) are ~3–5 hours on the nightside, >5 hours near dawn, 2 hours in the afternoon quadrant, and 2 hours at dusk.

2.3. Loss Rates

[17] We take account of loss due to precipitation as the electrons drift. In this study we consider two different models for electron pitch-angle scattering. Model 1 corresponds to the limiting idealization of strong pitch-angle

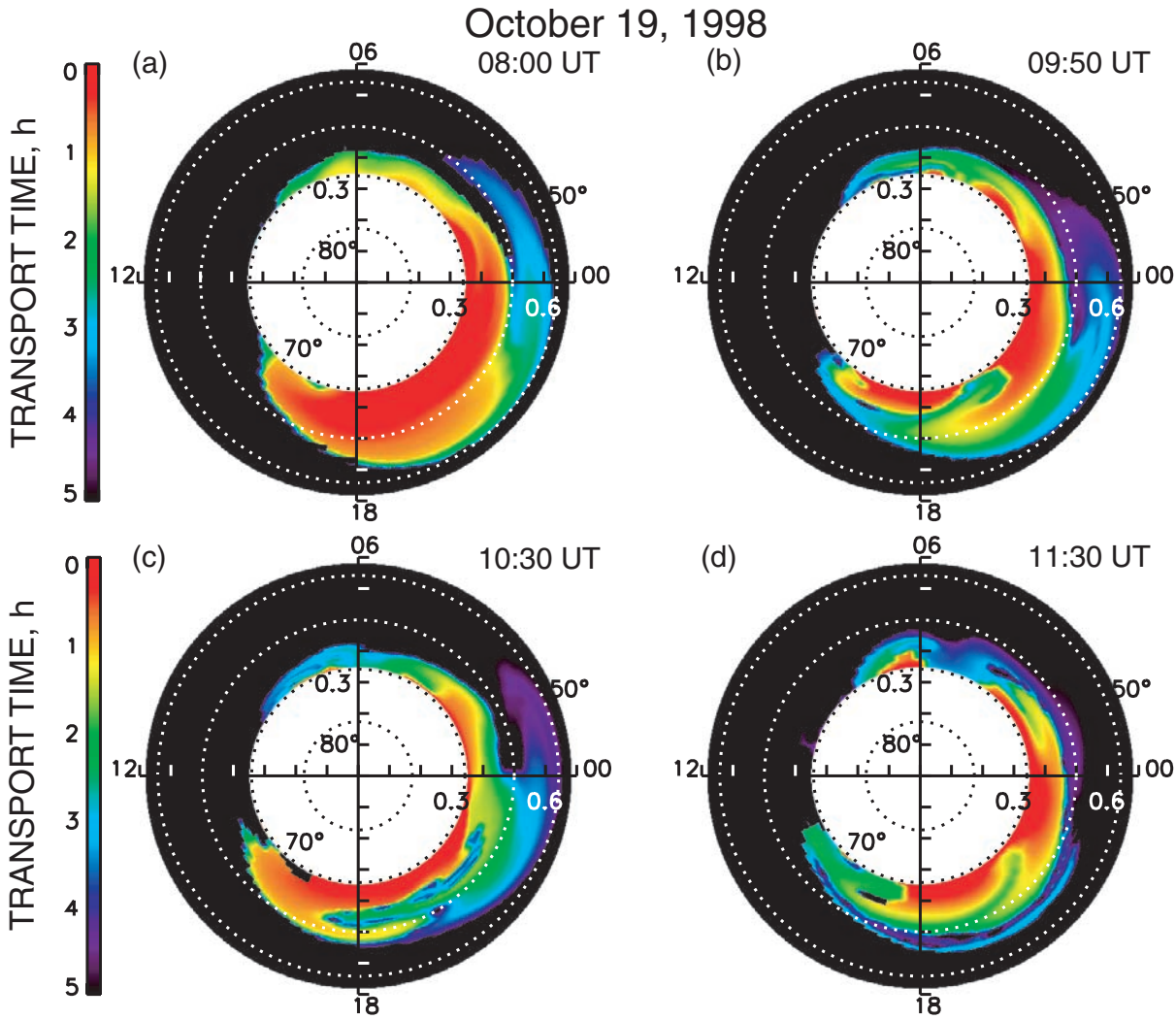

Figure 4. Simulated drift times required for plasma sheet electrons to reach ionospheric magnetic latitudes (at altitude 127.4 km) and magnetic local times of interest from the nightside neutral line at (a) 0800 UT, (b) 0950 UT, (c) 1030 UT, and (d) 1130 UT.

diffusion everywhere but with an adjustable backscatter coefficient [*Chen and Schulz*, 2001a]. Model 2 is based on the less than everywhere strong scattering model 2 of *Chen and Schulz* [2001b] but with a prescribed dependence on MLT. In this study, we directly compare auroral observations with simulated distributions of precipitating electron energy flux and emitted X-ray flux obtained from these two scattering models, so as to infer realistic estimates of scattering rates.

2.3.1. Loss Due to Strong Pitch-Angle Diffusion (Model 1)

[18] The lifetime τ against strong pitch-angle diffusion can be expressed [*Schulz*, 1974a] as

$$\tau = (\gamma m_0/p)[2\Psi B_h/(1-\eta)], \qquad (9)$$

where the quantity B_h in (9) denotes the field intensity at either foot point of the field line of interest in a centered-dipole model, and the factor $\gamma(=m/m_0)$ denotes the ratio of the relativistic mass m to the rest mass m_0 for the particles of interest. The backscatter coefficient η is an adjustable parameter of the model. For this study we specify $\eta = 0.25$ (independent of incident electron energy) so that 25% of the electrons that would mirror at or below the altitude $h(=0.02\ R_E)$ are scattered back into the flux tube instead of precipitating into the atmosphere. Figure 5 shows (Figure 5a) equatorial and (Figure 5b) polar projections of the lifetime against strong pitch-angle diffusion for electrons having $\Lambda = \Lambda_4$. From Figure 5a one can see that the strong-diffusion lifetime τ increases monotonically with R_0 at a given value of Λ because of the factor Ψ in (9). The lifetime against strong diffusion for 4-keV electrons at $R_0 = 6$ ($L \approx 5.7$ in the present field model, corresponding to 65° latitude in Figure 5b) is about 20 min. (See Plate 3 of *Chen and Schulz* [2001a] for plots of lifetime against strong pitch-angle diffusion

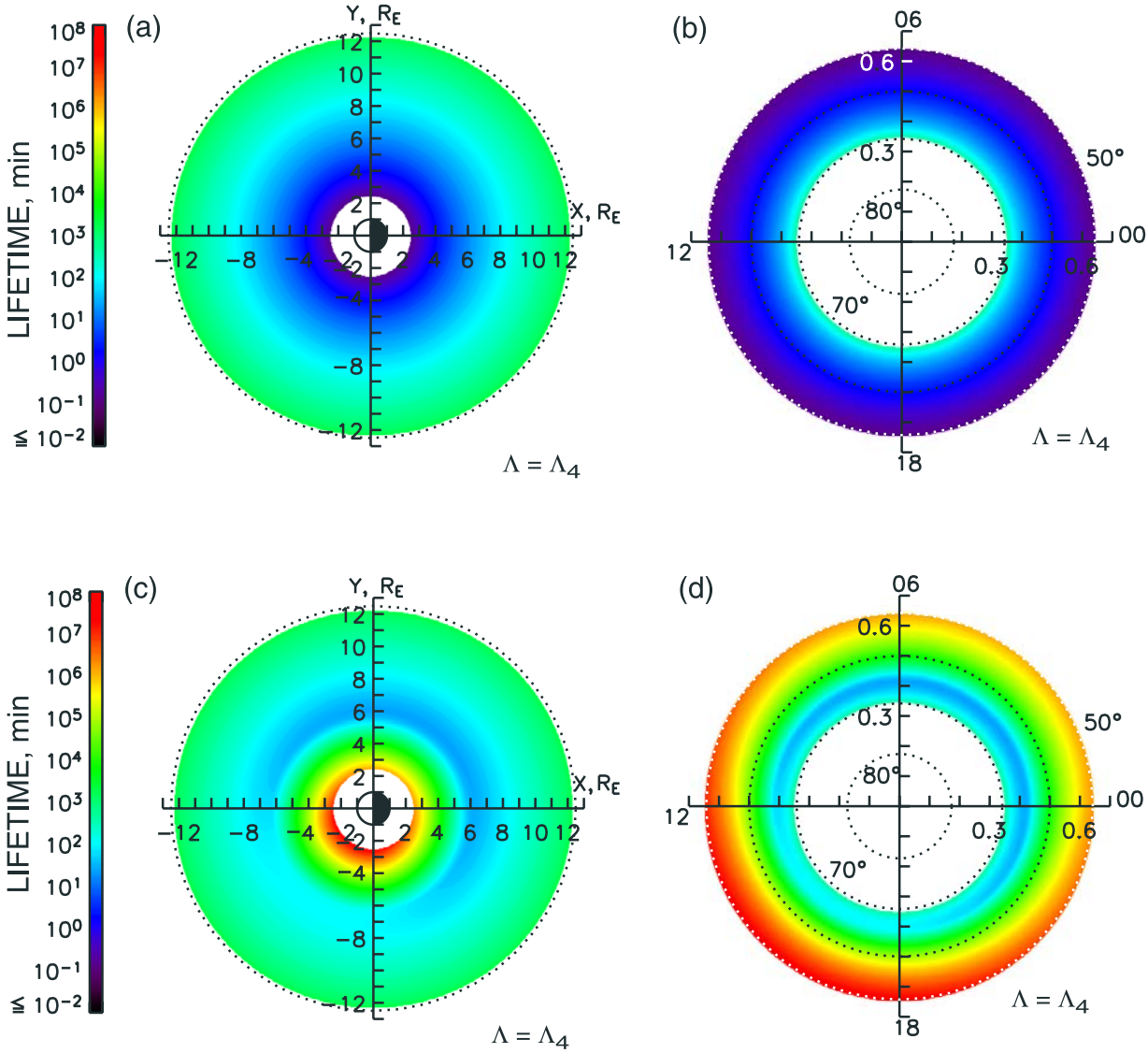

Figure 5. (a) Equatorial intercepts and (b) polar projections of the lifetime against strong pitch angle diffusion given by (9) for electrons with $\Lambda = \Lambda_4$. (c) Equatorial intercepts and (d) polar projections of the electron lifetime against MLT-dependent diffusion given by (11) and (12) for electrons with $\Lambda = \Lambda_4$.

versus R_0 for other Λ values corresponding to energies of 0.25 keV to 64 keV at $R_0 = 6$.)

2.3.2. A Model for MLT-Dependent Pitch-Angle Diffusion Less Than Everywhere Strong (Model 2)

[19] Strong pitch-angle diffusion is a limiting idealization. Some observations [e.g., *Stiles et al.*, 1978] show nearly isotropic plasma sheet pitch-angle distributions, but other particle observations [*Fairfield and Viñas*, 1984; *Schumaker et al.*, 1989] and wave measurements [*Gough et al.*, 1979; *Belmont et al.*, 1983; *Roeder and Koons*, 1989; *Koons and Roeder*, 1990; *Meredith et al.*, 1999, 2000] suggest that pitch-angle scattering may not always be strong throughout the plasma sheet. Our previous simulations [*Chen and Schulz*, 2001a] of storm time diffuse aurora with plasma sheet electrons in strong pitch-angle diffusion also show the need for a model in which plasma sheet pitch-angle diffusion is less than everywhere strong.

[20] Unfortunately, there are very few (if any) reported measurements of electron lifetimes in the plasma sheet, especially at energies (~0.1–100 keV) of interest in this study. In an earlier study we formulated a model for pitch-angle diffusion less than everywhere strong. This model was based on theoretical electron lifetimes against weak diffusion [*Albert*, 1994] intended for application to radiation-belt electrons. For application to plasma sheet electrons we extrapolated Albert's results to higher L values and lower energies. Then we renormalized to match empirical lifetimes [*Roberts*, 1969; *Van Allen*, 1969]. The scattering rate λ that we thus obtain is well approximated by the expression

$$\lambda_0(E,L) = \min\left[0.08(E,\mathrm{MeV})^{-1.32},\ 0.4\times 10^{(2L-6+0.4\log_2(E))}\right]\ \mathrm{day}^{-1}, \quad (10)$$

where energy E is measured in units of MeV. (Our equation (10) here corrects a typographical error in equation (5a) in the paper of *Chen and Schulz* [2001b], which provides specific details on how this scattering-rate

model was formulated.) The scattering rate approximated by (10) pertains only to wave-particle interactions. Coulomb scattering has been treated by *Walt* [1964], *Lyons and Thorne* [1973], and *Abel and Thorne* [1998] but we neglect it here because the theoretical lifetimes of *Lyons and Thorne* [1973] show that lifetimes against wave-particle interactions are significantly shorter than those against Coulomb scattering beyond $L \sim 3.5$ for energies of 10–20 keV. For example, a 10-keV electron at $L = 5$ has a Coulomb lifetime of ~100 days, whereas (1) yields a lifetime ~2.7 hours against wave-particle interactions.

[21] Observations of wave activity in the equatorial magnetosphere indicate that the scattering rate depends on MLT as well as on R_0. For example, *Koons and Roeder* [1990] surveyed ELF/VLF wave activity in the frequency range 0.1–5 kHz detected by the SCATHA satellite's VLF receiver near the magnetic equator at $r \approx 5$–$8\ R_E$. Hiss, discrete whistler mode emissions, and electron cyclotron harmonic waves (ECH) occur within this frequency range. *Koons and Roeder* [1990] reported the probability of detecting wave activity above the threshold of SCATHA's broadband VLF receiver as a function of R_0 and MLT. They found that wave activity was notably absent from 1800 to 2100 MLT and relatively abundant from 0300 to 1200 MLT. The SCATHA wave data have not yet been analyzed statistically to reveal the mean amplitude or mean intensity as a function of L and MLT. Recently, J. L. Roeder (private communication, 2004) analyzed SCATHA wave amplitudes in the frequency range of 0.1–1.0 Hz for two large magnetic storms. He found that the MLT distribution of amplitudes ($\geq 5 \times 10^{-4}$ mV/m) during these storms to be consistent with the MLT distribution of the statistical surveys [*Roeder and Koons*, 1989; *Koons and Roeder*, 1990]. During the main phases of these two storms, the most largest wave amplitudes tended to occur around 0400 MLT.

[22] Motivated by such wave observations, we have modeled the MLT-dependence of the scattering rate so that

$$\lambda(E, L, \phi) = [1 + a_1 \sin(\phi + \phi_0) + a_2 \cos 2(\phi + \phi_0)]\lambda_0(E, L), \tag{11}$$

where $\lambda_0(E, L)$ is the azimuthally averaged scattering rate specified by (10) and φ is the MLT coordinate. The coefficients a_1, a_2, and φ_0 are adjustable parameters in this truncated Fourier expansion. In our earlier work we modeled the MLT dependence of the scattering rate $\lambda(\varphi)$ directly from the SCATHA wave occurrence frequency distribution of *Koons and Roeder* [1990] with $a_1 = 0.8$, $a_2 = 0$, and $\varphi_0 = -\pi/4$. In that model $\lambda(\varphi)$ reached a maximum value (=1.8 λ_0) at φ = 0900 MLT and reaches a minimum value(=0.2 λ_0) at φ = 2100 MLT around any magnetic shell. (See *Chen and Schulz* [2001b] for further details on this formulation.) With that MLT-dependent scattering rate we accounted qualitatively for intensifications of diffuse auroral electron precipitation found near dawn and late in the morning quadrant in both statistical and storm event studies [*Chen and Schulz*, 2001b]. In this study we find it revealing to adjust the parameters a_1, a_2, and φ_0 to obtain somewhat better agreement between the azimuthal distribution of simulated electron precipitation patterns and those inferred from averaged NOAA electron precipitation data and storm time Polar (UVI and PIXIE) images (presented later). With $a_1 = 1.2$, $a_2 = -0.25 * a_1$, $\varphi_0 = \pi/6$ in (11), the scattering rate $\lambda(\varphi)$ reaches a maximum value (=2.6 λ_0) peaking at 0400 MLT and a broad minimum value (=0.6 λ_0) at 2200 MLT. This produces less scattering in the evening and more scattering in the morning, which is consistent with both the storm time results of J. L. Roeder (private communication, 2004) and with the statistical results of *Koons and Roeder* [1990].

[23] A simple model [*Schulz*, 1979b] for the loss rate $\bar{\lambda}(\varphi)$, providing a smooth transition between weak pitch-angle diffusion ($\lambda\tau \ll 1$) and strong diffusion ($\lambda\tau \gg 1$), is

$$\bar{\lambda}(\varphi) = [1 + \lambda(\varphi)\tau]^{-1}\lambda(\varphi), \tag{12}$$

where τ is the lifetime against strong diffusion. The color-coded lifetime $1/\bar{\lambda}$ for electrons with $\Lambda = \Lambda_4$ is shown in Figure 5c as a function of (R_0, φ) and equivalently in Figure 5d as a function of (θ_h, φ) at $r = a + h$. For $R_0 > 9$, the lifetime approximates that found in the limit of strong pitch-angle diffusion (cf. Figures 5a and 5c). For $R_0 < 4$, the lifetimes $1/\bar{\lambda}$ in Figure 5 correspond approximately to the limit of weak pitch-angle diffusion regardless of MLT. At $R_0 = 6$, however, the lifetime range of $1/\bar{\lambda}$ specified by (12) for a 4-keV electron ranges from 25 min at 0400 MLT (which is approximately equal to the strong-diffusion lifetime) to 3.8 hours at 1600 MLT (which is approximately equal to the weak diffusion limit).

2.4. Phase Space Mapping

[24] Having treated plasma sheet electrons for kinematic purposes as if they were in strong diffusion, we map the storm time phase-space density f for each value of Λ according to Liouville's theorem, except that we attenuate f by the factor $\exp(-\int\bar{\lambda}dt)$ along each drift trajectory to account for the rate $\bar{\lambda}$ specified by (12) at which electrons are lost from their respective flux tubes because of pitch-angle scattering. This approach represents a kinematical compromise that we believe is well justified (see below). Under strong pitch-angle diffusion, the differential omnidirectional electron flux $J_{4\pi}$ for any value of Λ would be instantaneously uniform along any field line of interest, and so we could identify $f = J_{4\pi}/4\pi p^2$ as in our earlier work [*Schulz and Chen*, 1999; *Chen and Schulz*, 2001a]. This would constitute a form of adiabatic motion in which L (rather than the first two invariants M and J) is conserved. It is tantamount to the approach used in the Rice Convection Model (RCM) [*Harel et al.*, 1981].

[25] Our phase-space mapping differs from the approach of *Fontaine and Blanc* [1983], who computed the transport and precipitation of plasma sheet electrons in the limit of strong pitch-angle diffusion by using fluid equations. Assuming Maxwellian electron distributions and a uniform electron density in each flux tube, they solved the electron mass and energy conservation equations after imposing a prescribed temperature profile at their boundary (i.e., at L = 10 in a dipole field).

[26] We admit that we are making a kinematical compromise whenever pitch-angle diffusion is less than strong (as in scattering models 2 and 3). This point was discussed by *Chen and Schulz* [2001b]. The base for our kinematical compromise is that even in the absence of pitch-angle diffusion, particles starting with the same field line with

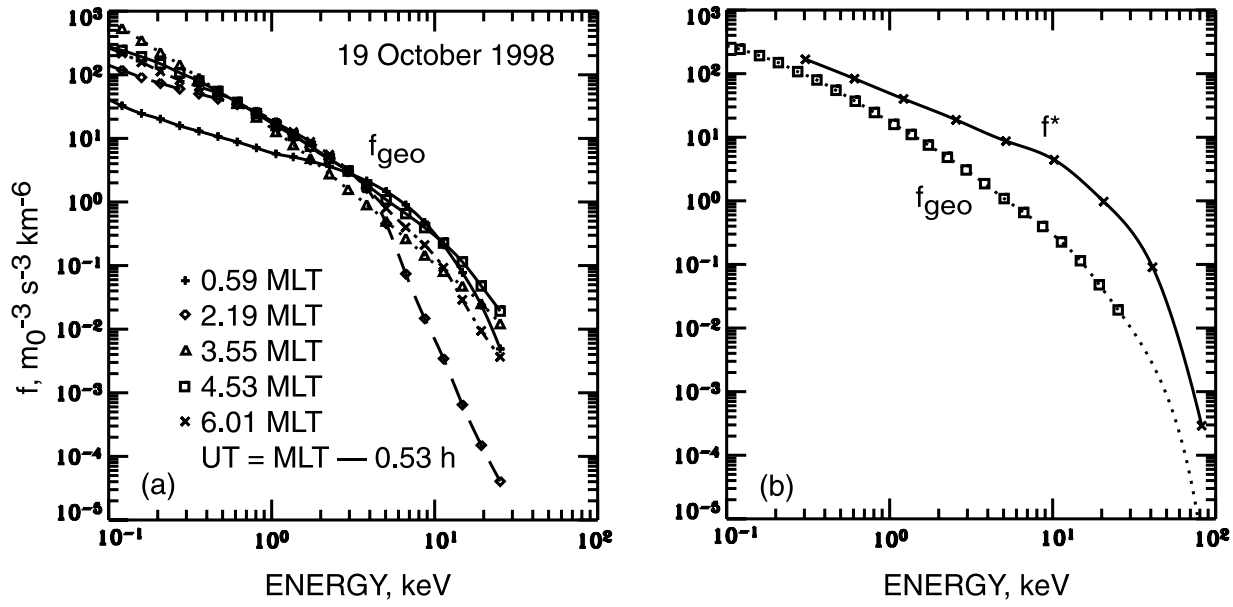

Figure 6. (a) Phase space spectra at geosynchronous altitude at different MLT and UT(=MLT − 0.53 hours) on 19 October 1998. Plotting symbols correspond to actual LANL/MPA data points while the curves are cubic-spline interpolations through the data points. (b) The geosynchronous phase space spectrum (square symbols and dotted curve) at 4.53 MLT and 0400 UT on 19 October 1998 is replotted in this panel. This spectrum is mapped to the boundary of our model and shown as the solid curve. The crosses correspond to the boundary phase space spectrum at eight different $\Lambda(=\Lambda_{0.25}, \Lambda_{0.5}, \Lambda_1, \Lambda_2, \Lambda_4, \Lambda_8, \Lambda_{16}$, and $\Lambda_{32})$ values.

the same energy but with different equatorial pitch angles (e.g., $\alpha_0 = 90°$ and $\alpha_0 = 0°$) would still drift at similar rates along similar paths [e.g., *Chen et al.*, 1998].

2.5. Boundary Conditions

[27] We use electron fluxes at geosynchronous orbit provided by the Magnetospheric Particle Analyzer (MPA) instruments on Los Alamos National Laboratory (LANL) satellites to construct our boundary conditions for *f*. The MPA is an electrostatic analyzer that measures three-dimensional energy per charge (∼1 eV/q to ∼40 keV/q) distributions of ions and electrons. See *Bame et al.* [1993] and *McComas et al.* [1993] for a complete description of the instrument. Figure 6a shows examples of LANL/MPA electron phase space spectra that correspond to five different MLT values, ranging from 0000 MLT to 0600 MLT on 19 October 1998. For each spectrum in Figure 6a the corresponding UT is 0.53 hours earlier than the MLT (UT = MLT − 0.53 hours) because this particular LANL satellite is located at 8°E geographic longitude. The symbols correspond to the actual LANL data, while the curves are cubic-spline interpolations through these points. Figure 6a shows considerable variability in the spectral hardness of the geosynchronous electron distribution with MLT and/or UT. The main phase of the 19 October 1998 storm started around 0500 UT. Unfortunately, the available LANL satellites were on the dayside through most times of interest (∼0800 UT to 1130 UT) during the main phase of the 19 October 1998 storm. They therefore do not necessarily provide a good representation of the nightside electron plasma sheet distributions. We select the phase space spectrum at 4.53 MLT as representative of geosynchronous orbit for this storm, realizing that this is an oversimplification of the true time-dependent storm time spectrum.

[28] We construct the phase space spectrum f^* at the boundary of our model at $L = L_c < L^* = 8.5466$, where L_c denotes the largest value of L for which electrons of specified L could gyrate without escaping across the neutral line. Determination of this critical value of L as a function of Λ is explained in detail by *Chen and Schulz* [2001a]. We map the selected phase-space spectrum from geosynchronous orbit outward to L, multiplying f by the factor exp $(\int (1/\tau)\, dt)$, where τ is the lifetime against strong diffusion given by (9). For simplicity, the time integral of $(1/\tau)$ is calculated along a trajectory from midnight at geosynchronous orbit to L_c. The equatorial radial distance with which we associate the LANL geosynchronous data in our axisymmetric magnetic field model is not $R_0 = 6.6$ but rather the distance $R_0 = 5.47$ where the equatorial magnetic field intensity equals that given by the empirically based magnetic field model of *Tsyganenko* [1989] for $Kp > 6-$ at $R_0 = 6.6$ at midnight. We think it is more appropriate to match the equatorial magnetic field value at which the observational data were probably acquired than to match the actual altitude of the satellite. Figure 6b shows the selected LANL geosynchronous electron phase-space spectrum (squares) at 4.53 MLT at geosynchronous (squares) and its mapping to $L = L_c$. We use the cubic spline interpolations (solid curves) to model smooth spectra for f and f^* in Figure 6.

3. Simulation Results

3.1. Energy Flux

[29] We compute the differential and integral energy flux distributions of electrons precipitating into the ionosphere from the mapped phase-space densities (for each of our three different electron scattering models) for the selected

times of interest during the 19 October 1998 storm. Our method for computing the differential and integral energy fluxes is explained in detail by *Chen and Schulz* [2001b]. Our integral energy flux is given by an integral of the differential energy flux over all energies. Here we compare the simulated energy fluxes with a statistically averaged distribution of electron energy flux based on NOAA measurements and with UVI images from NASA's Polar satellite.

[30] Spatial distributions of energy flux (color coded in units of erg cm^{-2} s^{-1}) are shown in Figure 7. Simulated energy fluxes for scattering rate model 1 (strong pitch-angle diffusion) for 19 October 1998 at 1030 UT and 1130 UT are shown in Figures 7a and 7b, respectively. Under strong pitch-angle scattering the simulated energy flux attains a maximum value of 29.0 erg cm^{-2} s^{-1} at 65.2° latitude and 2140 MLT at 1030 UT. At 1130 UT, the energy flux attains a maximum value of 40.2 erg cm^{-2} s^{-1} at 64.5° latitude and 2300 MLT. In both examples the most intense energy flux (red) in the evening quadrant at latitudes of ~63°–67° latitude. This is where the strong diffusion lifetimes (~20–30 min for 1–4-keV electrons) are comparable to the drift access times (~20–30 min) from the neutral line of the model (cf. Figures 4 and 5b). As in our earlier simulations, we find that the differential energy-flux spectrum peaks at energies ~4 keV at R_0 = 6 R_E. (We do not show such differential energy-flux spectra here, but examples from a different study are illustrated in Figure 1 of *Chen and Schulz* [2001b].) Thus the maximum energy flux corresponding to a match between the drift and loss timescales of 4-keV electrons are representative of the precipitating electron population. Because the lifetimes against strong pitch-angle diffusion are shorter than the transport times to the dayside magnetosphere, most electrons would have precipitated before they could drift around to the dayside.

[31] For comparison, we show the simulated distribution of energy flux obtained with scattering rate model 2 (MLT-dependent diffusion) for 19 October 1998 at 1030 UT and 1130 UT in Figures 7c and 7d. The region of energy flux >1 erg cm^{-2} s^{-1} tends to be more widely distributed in MLT under model 2 than under model 1 (strong diffusion). This makes sense, in that under the MLT-dependent scattering model more electrons are able to drift around to dawn and to the dayside with scattering rate model 2 because the lifetimes are generally longer there than under strong diffusion. The maximum energy flux (10.6 erg cm^{-2} s^{-1}) occurs at 63.9° latitude and 0420 MLT in Figure 7c. The maximum energy flux (11.3 erg cm^{-2} s^{-1}) is attained at 63.9° latitude and 0300 MLT in Figure 7d. These peak values are notably smaller than the corresponding peak values under strong diffusion. Conversely, the region of energy flux under scattering model 2 extends from premidnight to postdawn at ~63°–65° latitude. Our MLT-dependent scattering rate yields the shortest lifetimes around 0400 MLT (see Figures 5c and 5d). Although the pattern of precipitating energy flux tends to be more spread out in MLT under model 2 than under model 1, the total rate of energy deposition into the ionosphere at 127 km altitude is roughly the same under model 1 (4.81×10^{19} ergs/s) as under model 2 (4.87×10^{19} erg/s) at 1030 UT on 19 October 1998. The total rate of energy is calculated by integrating the integral energy flux over $r^2\, d(\cos\theta_h)\, d\varphi$ at $r = (a + h)$.

[32] To assess which scattering model produces the more realistic diffuse aurora, we compare our simulated energy-flux distributions with observed energy flux distributions. For orientation, we first examine 10-year averages of NOAA-12 energy flux data (for corresponding values of *Dst*) for electrons with energies ranging from 379 eV to 902 keV. The energy flux is derived from the Total Energy Detector (TED), an electrostatic analyzer, and the Medium Energy Proton and Electron Detector (MEPED), a solid-state detector, of the Space Environment Monitor. Details about the two NOAA-12 instruments can be found in the work of *Raben et al.* [1995]. Information regarding the generation of the NOAA-12 averaged precipitation flux can be found in the work of *Wüest et al.* [2005]. The electron data corresponding to the *Dst* bin from −80 nT to −110 nT are averaged over the 10-year period spanning 1 June 1991 through 31 July 2001. The times of interest during the main phase of the 19 October 1998 storm correpond to *Dst* values that fall within the −80 nT to −110 nT bin. Figure 7e shows a plot of the averaged NOAA-12 energy flux data in the southern hemisphere with the same color scale as the simulated energy flux plots in Figure 7. Data coverage was sparse at low latitudes from about 2200 MLT to 0300 MLT. Statistically, the averaged energy fluxes above 1 erg cm^{-2} s^{-1} tended to occur roughly between 1700 MLT to 0900 MLT.

[33] Comparing the simulated storm time energy flux under model 1 (Figures 7a and 7b) with the averaged NOAA data (Figure 7e), one can see that the simulated storm time energy flux with strong diffusion tends to be much more intense than what is statistically observed in the evening sector. In contrast, the simulated storm time energy flux under model 2 (Figures 7c and 7d) tends to have comparable magnitudes with the observed average energy fluxes although the maximum energy flux from the simulations is somewhat higher than the maximum 10-year average energy flux. The spatial extent of the simulated storm time energy flux under model 2 agrees quite well with the averaged NOAA data. Thus we conclude that the simulations with our MLT-dependent scattering rate produce a more realistic storm time diffuse aurora than does a model based on strong diffusion (at least in a statistical sense). Later, we will compare our simulated electron energy flux with the electron energy flux inferred from Polar/UVI images at selected times during the 19 October 1998 storm.

3.2. X-ray Flux

[34] For comparison with auroral Polar/PIXIE X-ray images, we also compute the simulated X-ray flux. To calculate the simulated X-ray flux, we need to apply what is known about the X-ray production by electrons incident the atmosphere. The thick target Brehmsstrahlung spectrum produced by incident electrons in the atmosphere was computed and the spectrum was multiplied by the detector efficiency and integrated over X-ray energies of 2 to 12 keV. We chose X-ray energies of 2 to 12 keV because this is the X-ray energy range of data collected from the front chamber of the PIXIE instrument that was used to produce the PIXIE images shown in this paper. (See a description of the instrument later in this section.) Figure 8 shows a plot of the intensity of 2–12 keV X rays [10^{-5}/cm^2 s sr] per electron differential number flux [1/cm^2 s sr] as a function of incident electron energy [keV]. Note that the X-ray

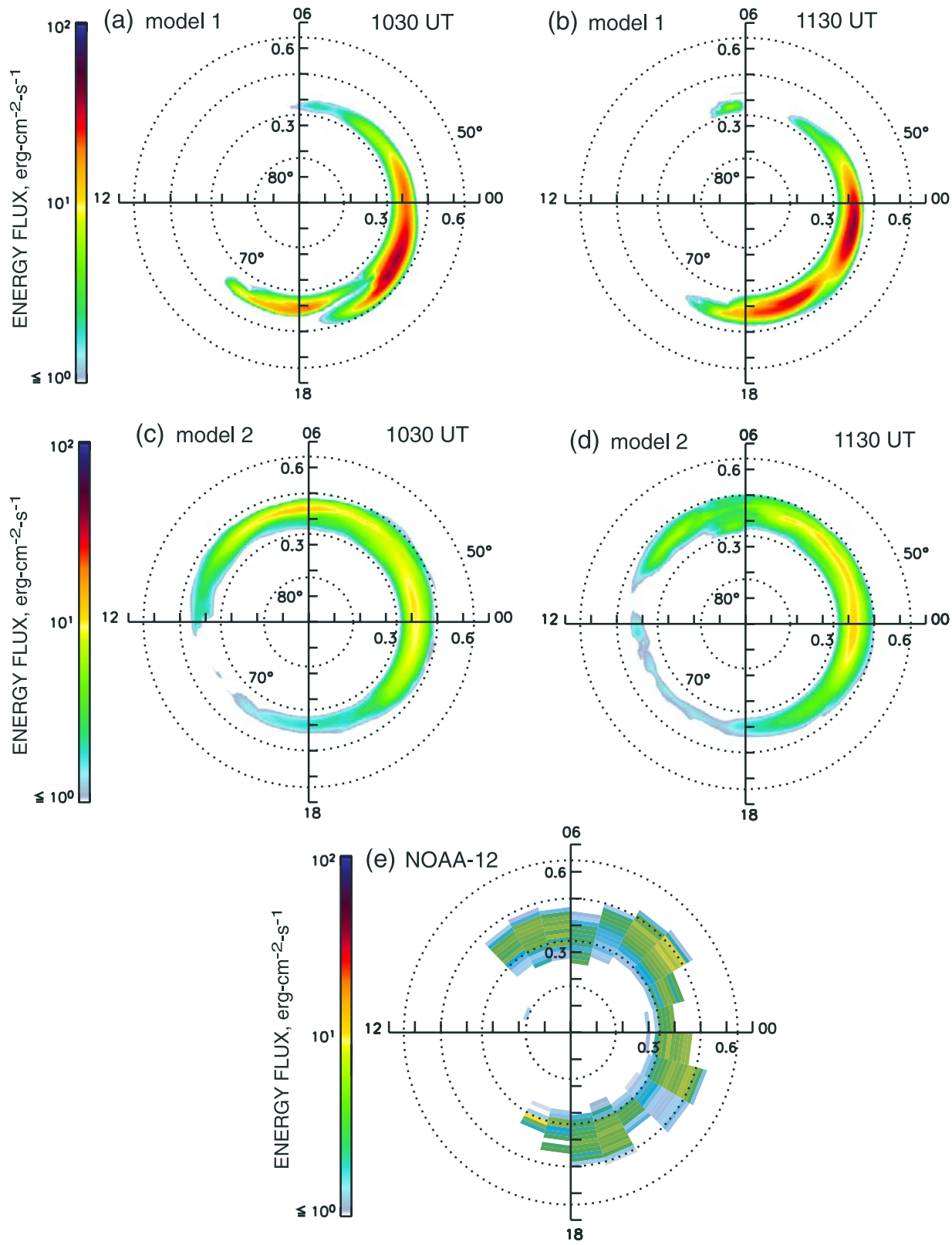

Figure 7. Polar plots of the simulated electron total precipitating energy flux on 19 October 1998 at 1030 UT (a) with strong diffusion (model 1) and (b) MLT-dependent diffusion (model 2), and at 1130 UT (c) with model 1 and (d) with model 2. (e) The 10-year average of the NOAA electron energy flux for $Dst = -80$ nT to -110 nT.

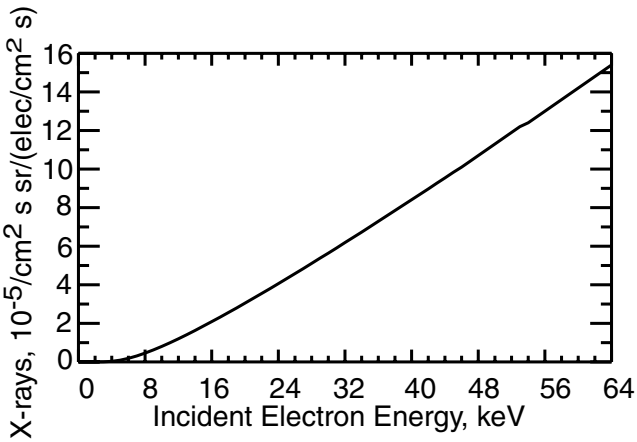

Figure 8. The X-ray production flux for 2–12 keV [10^{-5}/cm^2 s sr] per electron differential number flux [1/cm^2 s] versus the incident electron energy [keV].

production efficiency is very small for incident electron energies below 5 keV. The production efficiency increases monotonically with increasing incident electron energy. To compute the simulated X-ray intensity from the atmosphere for a given incident electron energy, we weight the simulated electron differential number flux with the X-ray production efficiency shown in Figure 8.

[35] Distributions of simulated X-ray intensity (2–12 keV) for 19 October 1998 at 3 selected times in units of cm^{-2} sr^{-1} s^{-1} are shown in Figure 9. The left column corresponds to scattering rate model 1 (strong pitch-angle diffusion). Simulated X-ray intensities computed with this model are too strong at the peaks and too narrowly distributed in MLT when compared (see next subsection) with PIXIE data. For example, model 1 yields a peak X-ray intensity of 1.8×10^4 cm^{-2} sr^{-1} s^{-1} (at 65.2° latitude and 2140 MLT) for 1030 UT (Figure 9b), and 2.8×10^4 cm^{-2} sr^{-1} s^{-1} (at 64.5° latitude and 2320 MLT) for 1130 UT (Figure 9c) on 19 October 1998. These maximum values exceed by factors ~2–3 the corresponding maximum X-ray intensities measured by PIXIE (see below). With scattering model 2, the maximum simulated storm time X-ray intensities are approximately smaller than those found with scattering model 1. The maximum simulated X-ray intensities are 8×10^3 cm^{-2} sr^{-1} s^{-1} (at 62.6° latitude and 0420 MLT) for 1030 UT (Figure 9e) and 9×10^3 cm^{-2} sr^{-1} s^{-1} (at 63.3° latitude and 0320 MLT) for 1130 UT (Figure 9d). These maximum values are similar to the corresponding maximum X-ray intensities observed by PIXIE at these times (see below).

3.3. Comparisons of Simulation Results With Auroral Images

[36] In Figures 10–12 we compare our simulation results from the MLT-dependent scattering model 2 directly with auroral images taken from the Polar satellite during the main phase of the 19 October 1998 storm using PIXIE and UVI images. *Anderson et al.* [2000a, 2000b] reported on the global auroral X-ray and ultraviolet morphology of the 19 October 1998 storm. In this paper we focus on comparing our simulation results with auroral images in order to assess what observed features can and cannot be explained by our model. Thus our description of the instrumentation and data analysis will be very brief.

[37] Polar's ultraviolet imager (UVI) consists of a three-mirror optical system with several filters and an intensified-CCD detector [*Torr et al.*, 1995]. Two filters cover the far-ultraviolet Lyman-Birge-Hopfield N_2 emission band: the LBHs (s = short, 140–160 nm) and the LBHl (l = long, 160–180 nm). In this paper we show images from the LBHl filter. At LBHl wavelengths the atmospheric Schumann-Runge (O_2) absorption is negligible. Thus the emission intensity for LBHl is directly correlated with the total precipitating electron energy flux. The UVI field-of-view does not cover the entire oval; UVI was primarily imaging the morningside aurora throughout the main phase of the 19 October 1998 storm. Figure 10a shows the electron energy flux derived from the UVI image at 0948:37 UT on 19 October 1998. The black circles indicate magnetic latitudes 80°, 70°, 60°, and 50°. Figure 10a shows that the region of inferred electron energy flux greater than 10 erg cm^{-2} s^{-1} extends at least from 2000 MLT through midnight past dawn and around to the dayside.

[38] For comparison, Figure 10b shows the distribution of simulated electron energy flux from scattering rate model 2 at 0950 UT on 19 October 1998 on the same logarithmic color scale. The simulated electron energy flux exceeds 10 erg cm^{-2} s^{-1} from about 2000 MLT through midnight to about 1000 MLT, which is in good agreement with the UVI observations (Figure 10a). We admit that our simulations do not take into account the effect of discrete auroral arcs. Thus the UVI data may well show intensifications of the electron energy flux at high latitudes that our simulations may not reproduce. Indeed, the UVI image in Figure 10a shows intensification of energy flux 20 erg cm^{-2} s^{-1} (extending from ~65° magnetic latitude (MLAT) at 2300 MLT to ~64° MLAT at 0100 MLT) that the simulations do not fully reproduce. Our simulations also do not currently take into account the effect of the proton aurora that contributes to the auroral emissions within the UVI filter response. Since protons drift eastward, it is expected that the protons would likely precipitate in the dusk to midnight sector. The UVI energy flux is somewhat more intense in the pre-midnight sector near the equatorward part of the oval than the simulated energy flux. Nonetheless, the simulated and UVI derived energy flux agree well in the overall strength and azimuthal extent at this time (0950 UT) during the main phase of the storm.

[39] PIXIE is a multiple-aperture pinhole camera designed to image the entire auroral oval in X rays of energy 2–60 keV. For descriptions of the PIXIE instrument, see *Imhof et al.* [1995] and *Anderson et al.* [2000a]. The PIXIE images presented in this paper are produced from data taken from PIXIE's front chamber, which receives X rays of energy 2–12 keV (PIXIE's rear chamber, 10–60 keV, had failed on 27 September 1998.). Figure 10c shows an image of the integrated X-ray intensities observed by PIXIE that were accumulated from 0948:38 UT to 0950:30 UT on 19 October 1998. The projected geographic location of each photon was calculated assuming a 100-km source altitude and was converted to magnetic coordinates by using the International Geomagnetic Reference Field, 1995 (IGRF95). The noon-midnight and dawn-dusk MLT meridians are marked by

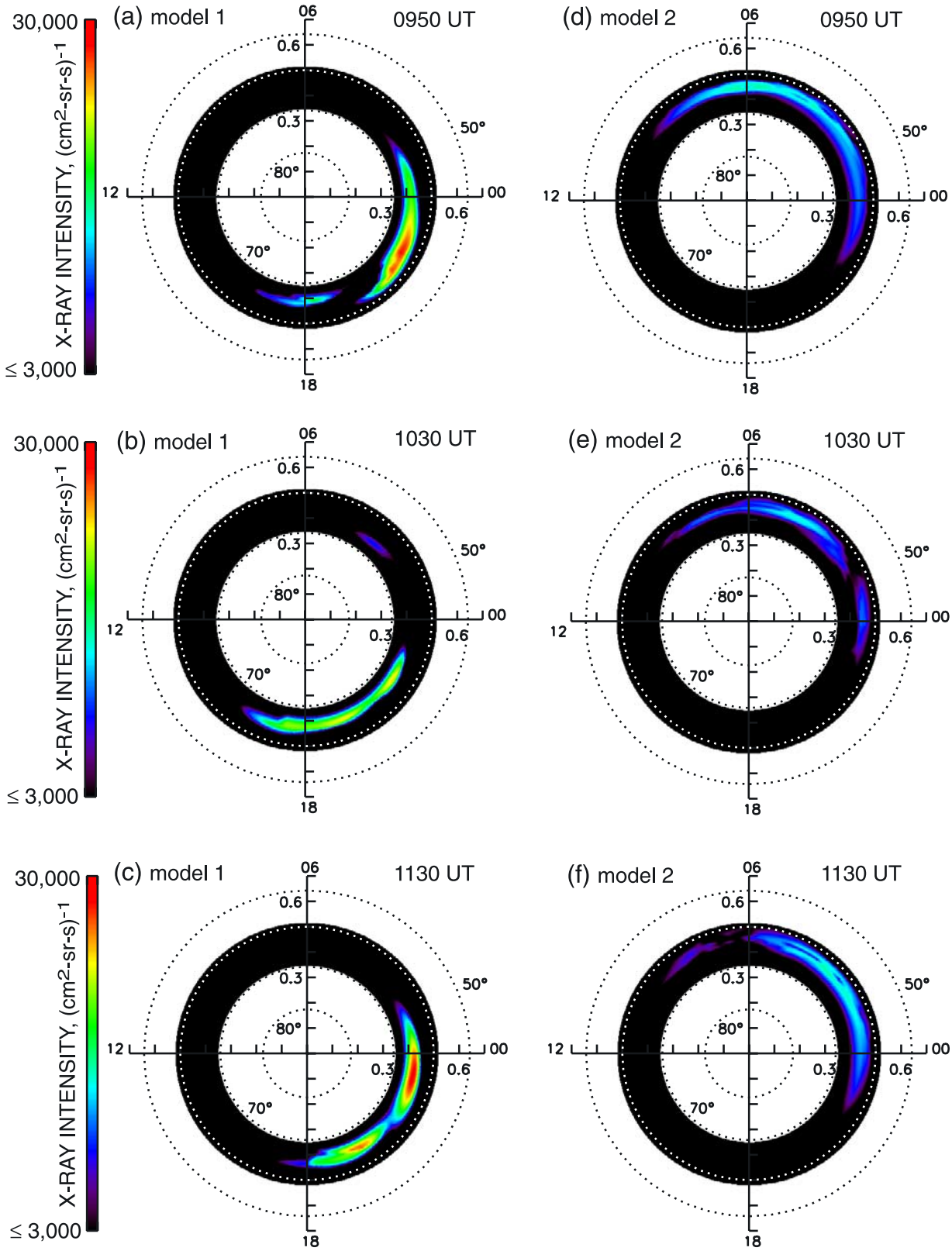

Figure 9. Polar plots of the simulated X-ray intensity on 19 October with strong diffusion (model 1) at (a) 0950 UT, (b) 1030 UT, and (c) 1130 UT; and MLT-dependent diffusion (model 2) at (d) 0950UT, (e) 1030 UT, and (f) 1130 UT.

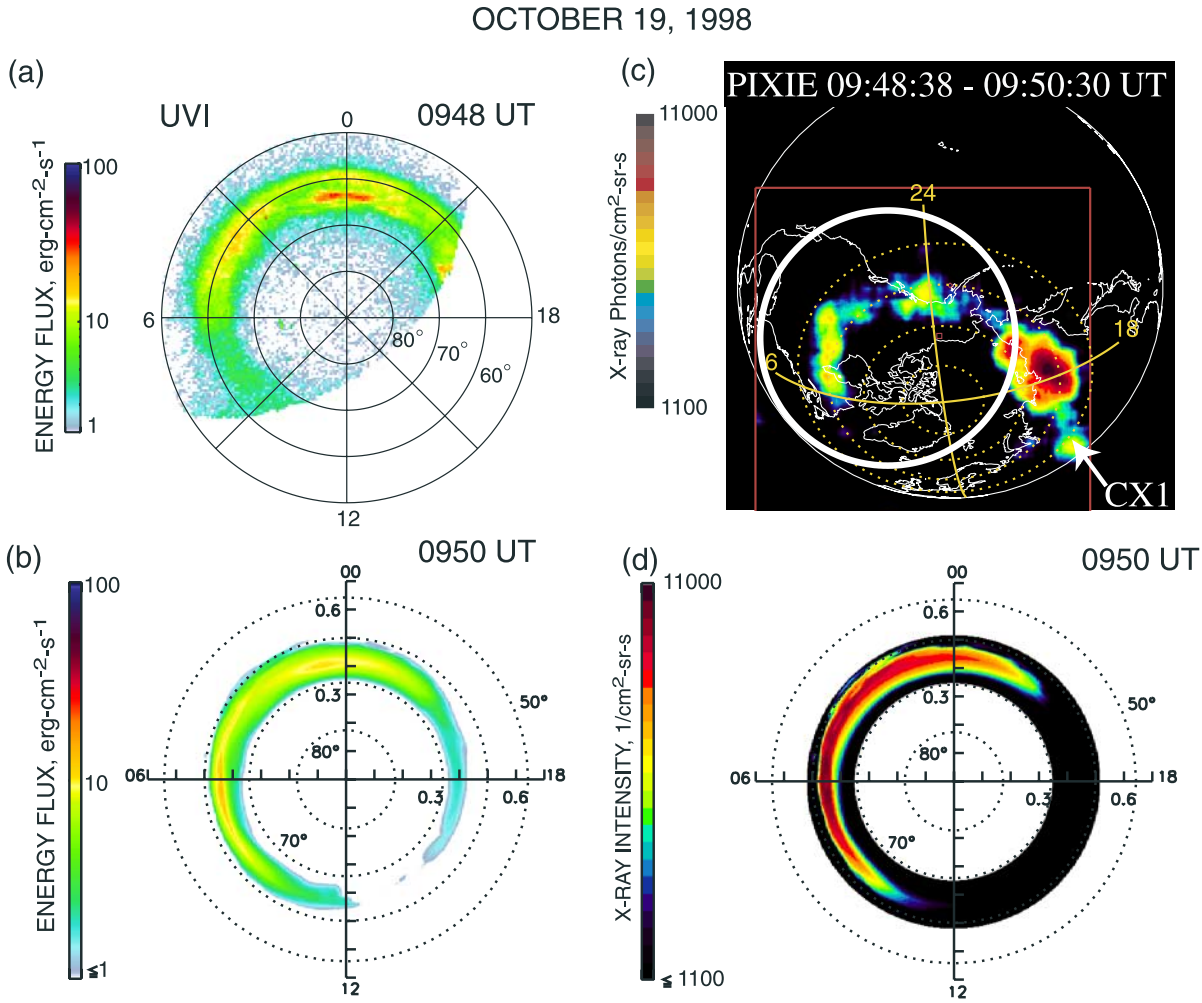

Figure 10. (a) Image of the UVI electron energy flux at 0948 UT. (b) Simulated electron energy flux at 0950 UT on 19 October 1998. (c) PIXIE X-ray image for 0948 to 0950 UT on 19 October 1998. The noon-midnight and dawn-dusk MLT meridians are marked by the solid yellow lines. The lines of constant MLAT are indicated by the dashed yellow lines. The bold white circle shows the field-of-view of the UVI image. (d) Simulated X-ray image at 0950 UT on 19 October 1998.

the solid yellow curves in Figure 10c. Contours of constant magnetic latitude (MLAT) are shown as dotted yellow curves. The imaged area is within the red box. For reference, the white circle in Figure 10c shows the field of view of UVI. The PIXIE image shows X-ray intensities >1100 cm^{-2} s^{-1} sr^{-1} at a region extending from ~1800 MLT through midnight to dawn, with the highest X-ray intensities near dusk. The "CXI" label refers to the aliased astronomical X-ray source Cirinus X-1. CXI is a point source, and so its image reveals spatial resolution. *Anderson et al.* [2000a] pointed out the enhancement of X-ray brightness at dusk (cf. Figure 10c) and discussed this feature in detail. They found that the geosynchronous Los Alamos National Laboratory (LANL) satellites measured enhanced electron fluxes in the pre-dusk region at the same time when PIXIE observed enhanced X-ray emissions in the postdusk region. *Anderson et al.* [2000a, 2000b] suggested that partially localized pitch-angle scattering and field-aligned electron acceleration might account for the intensification of the X-ray emissions in the postdusk region.

[40] Figure 10d shows the distribution of simulated X-ray intensity for scattering rate model 2 for comparison with the PIXIE X-ray image in Figure 10c. The simulated X-ray intensity exceeds 1100 cm^{-2} s^{-1} sr^{-1} from roughly 2200 MLT to the dayside at 1000 MLT. The simulated X-ray intensity for scattering-rate model 2 does not reproduce high X-ray intensities seen near dusk in Figure 10c; the brightest simulated X-ray fluxes occur between midnight and postdawn. With strong pitch-angle scattering everywhere as in scattering-rate model 1 (see Figure 9a, noting the different color bar scale), the simulated X-ray intensity is highest at 2100–2300 MLT near dusk and shows a secondary maximum (still over twice the observed maximum) near dusk. Simulations with scattering-rate model 1 would not account for the >1100 cm^{-2} s^{-1} sr^{-1} X-ray intensity between premidnight to dawn that is observed by PIXIE. Thus the simulated X-ray intensities with scattering-rate models 1 or 2 do not agree well with the PIXIE observations for this time of interest. This finding is consistent with the suggestion of *Anderson et al.* [2000a, 2000b] that the intense X-ray emissions in the

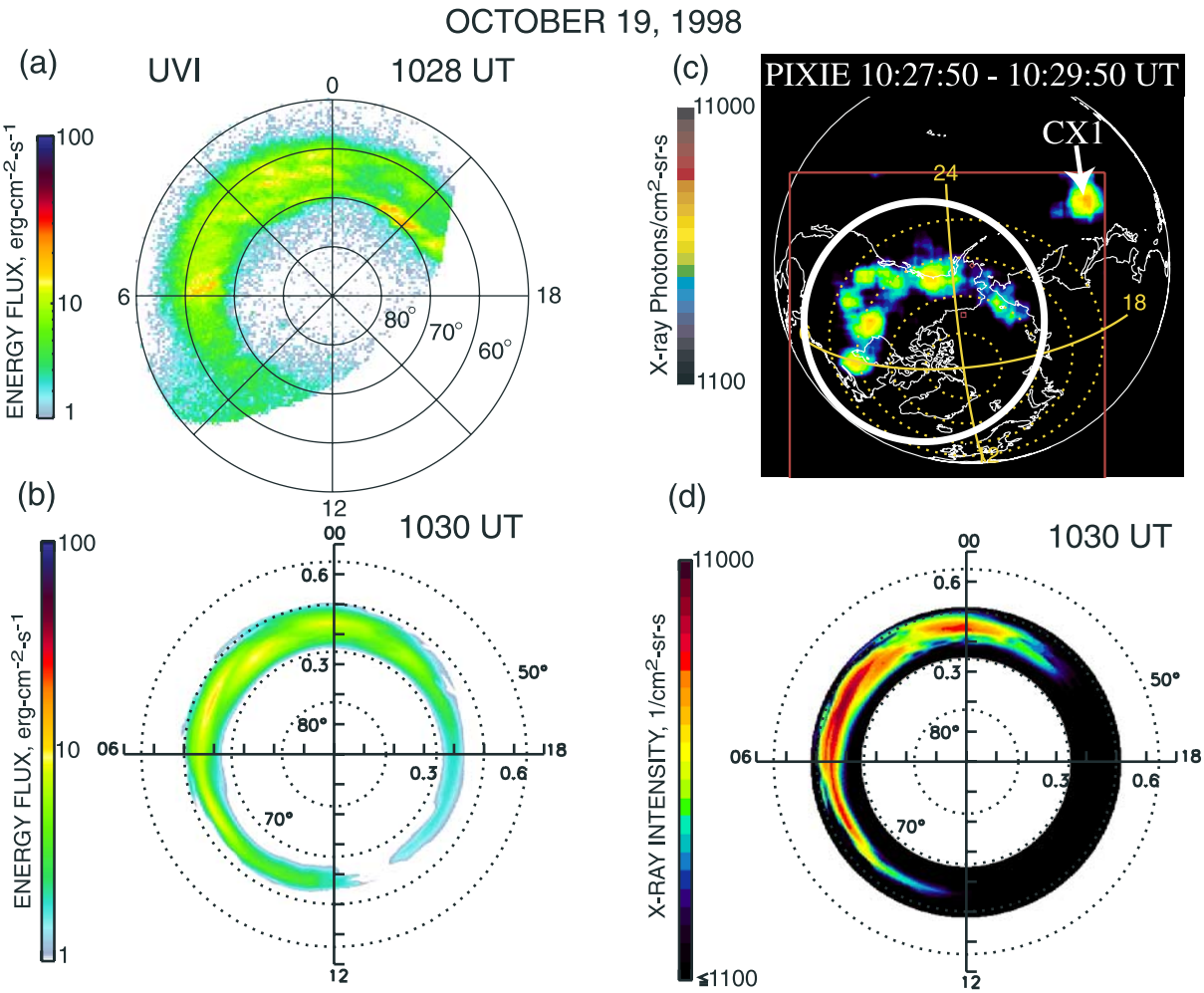

Figure 11. (a) Image of the UVI electron energy flux at 1028 UT. (b) Simulated electron energy flux at 1030 UT on 19 October 1998. (c) PIXIE X-ray image for 0927 to 0930 UT on 19 October 1998. (d) Simulated X-ray image at 1030 UT on 19 October 1998.

postdusk region might be due to partially localized pitch-angle scattering (i.e., preferentially scattered near dusk) and field-aligned acceleration mechanisms, neither of which are considered in our model.

[41] Comparisons between the "observed" and modeled storm time precipitating energy flux and X-ray intensity at 1030 UT on 19 October 1998 are shown in Figure 11. The simulation results shown correspond to those with scattering-rate model 1. The simulated precipitating electron and UVI energy fluxes in Figure 11b agree well with those inferred from the UVI image in Figure 11a, both in overall distribution in longitude and in order of magnitude. As expected, the simulated precipitating electron energy flux fails to reproduce some of the high-latitude intensifications observed in the UVI images, presumably because our model presently does not account for field-aligned acceleration of particles associated with discrete aurora arcs. The longitudinal distributions of simulated (Figure 11d) and observed (Figure 11c) X-ray intensity agree fairly well. The region of PIXIE X-ray intensity >1110 cm^{-2} s^{-1} sr^{-1} extends from roughly 2000 MLT through midnight to 0600 MLT, whereas the simulated X-ray intensity >1110 cm^{-2} s^{-1} sr^{-1} extends from roughly 2000 MLT through midnight to about 1100 MLT. Moreover, the latitudinal distribution of X-ray intensity seen by PIXIE is similar to the latitudinal distribution of energy flux inferred from UVI. Our simulations can reproduce part of the latitudinal distribution of the observed X-ray brightness. The regions of simulated and observed X-ray intensities >1110 cm^{-2} s^{-1} sr^{-1} extends from 70° to 60° latitude between midnight and dawn. However, the region of simulated X-ray intensity >1100 cm^{-2} s^{-1} sr^{-1} does not reach to as low a latitude (~50° latitude near ~0400 MLT) as in the PIXIE image. This may be because the AMIE electric field underestimates the storm time electric field intensity at low latitudes at this time. A stronger electric field at low latitudes could lead to transport of the plasma sheet electrons to lower latitudes. Moreover, the simulated X-ray intensity attains a higher maximum value than what is observed. Overall, there is good agreement between the simulated energy flux and that inferred from UVI measurements but only fair agreement between the simulated and PIXIE X-ray intensities in Figure 11.

[42] Finally, Figure 12 corresponds to 1130 UT on 19 October 1998. For this case the latitudinal distributions of simulated precipitating electron energy flux and X-ray intensity agree fairly well with the corresponding UVI-inferred electron energy flux and PIXIE measured X-ray intensity. The UVI-inferred electron energy flux peaks near

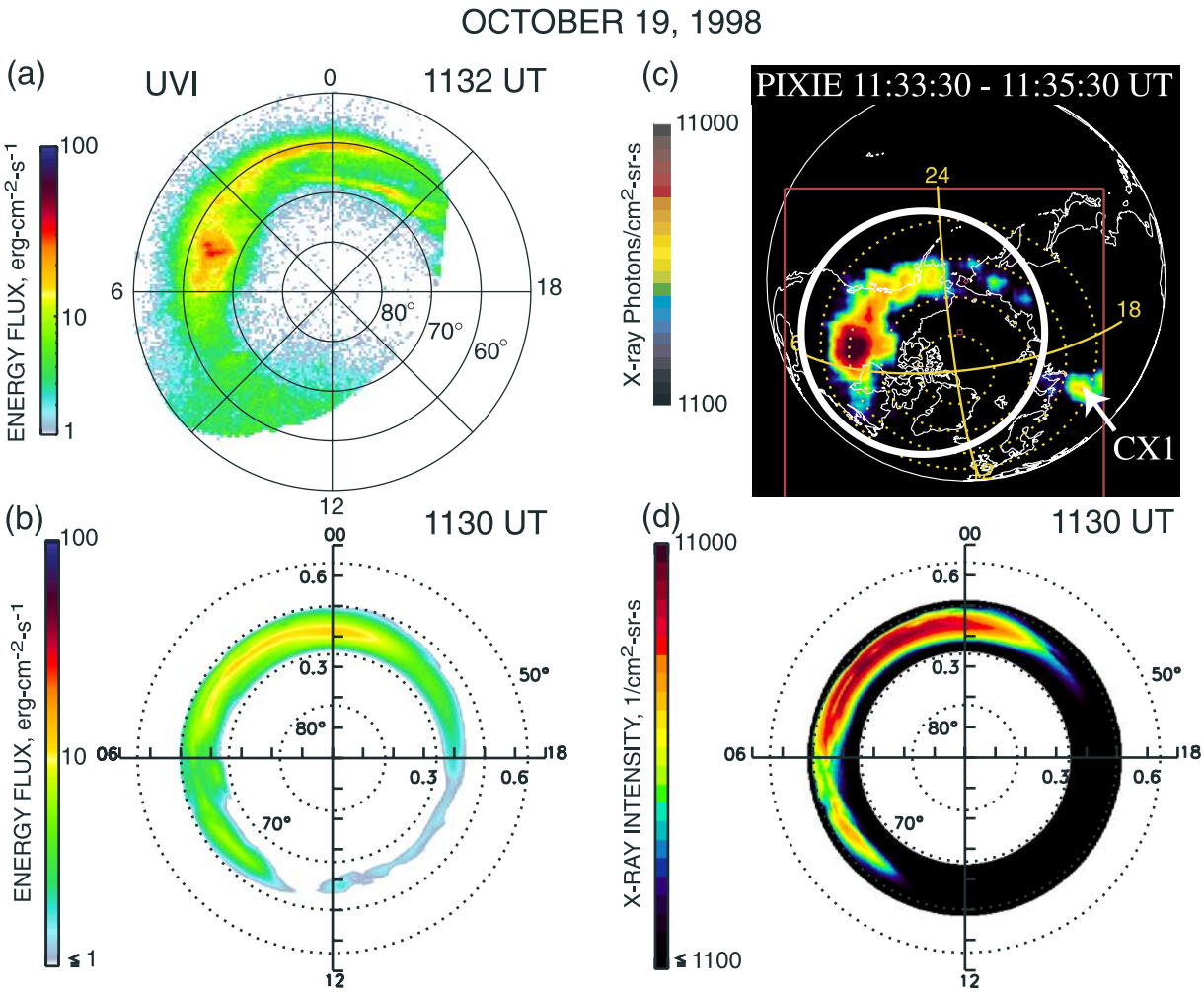

Figure 12. (a) Image of the UVI electron energy flux at 1133 UT. (b) Simulated X-ray intensity at 1130 UT on 19 October 1998. (c) PIXIE X-ray image for 1133 to 1135 UT on 19 October 1998. (d) Simulated X-ray image at 1130 UT on 19 October 1998.

0500 MLT, whereas the simulated energy flux peaks at 0300 MLT. Again, the simulations do not reproduce intensification in the UVI-inferred electron energy flux seen at high latitudes in the premidnight sector (probably associated with discrete auroral arcs). The PIXIE region X-ray intensity >1100 cm^{-2} s^{-1} sr^{-1} extends to lower latitudes at dawn (~53°) than at dusk (~60°). This is as expected since electrons are transported to lower L values as they drift eastward toward dawn from the nightside plasma sheet. The simulated X-ray intensity distributions show a similar trend. At dawn, however, the simulated >1110 cm^{-2} s^{-1} sr^{-1} X-ray intensity extends only to ~61° latitude (not as low as the PIXIE observations show). Nevertheless, the similarity in the azimuthal distribution of the observed and simulated X-ray intensity and precipitating energy flux for this example is encouraging. From this numerical experiment, we have postulated the MLT dependence of the scattering rate that wave scattering is weak in the post dusk sector (minimum at 2200 MLT) and strong in the morning sector (maximum at 0400 MLT). Both storm time (J. L. Roeder, private communication, 2004) and statistical [*Koons and Roeder*, 1990] analyses of SCATHA wave data indicate that the observed wave activity is strongest in the morning sector and weakest in the postdusk sector.

4. Summary and Conclusions

[43] In this study we have compared simulated and measured distributions of precipitating diffuse auroral electron energy flux and emitted X-ray brightness for the 19 October 1998 storm. Distributions of the simulated electron energy flux and X-ray intensity have been computed from phase-space mapping simulations of plasma sheet electrons with two scattering models: (1) strong diffusion and (2) MLT-dependent diffusion that is less than everywhere strong. We have compared the simulated electron energy flux distributions using these two different scattering models with statistically averaged NOAA-12 precipitating electron data (for $Dst = -80$ nT to -110 nT) and Polar/UVI images, and the simulated X-ray intensity distributions with Polar/PIXIE images. The distributions of precipitating electrons during magnetic storms depend on variations of the source distribution (i.e., magnetotail electron fluxes), electron transport, and electron pitch-angle scattering. All these

effects are important. The variations in source distribution, that is, the magnetotail electron fluxes, during storms certainly place an upper limit on how much precipitating electron energy flux would be available during the storm. The convection electric field enhances the inward transport of electrons during storms. However, the comparisons of simulated and observed distributions presented in this paper show that electron pitch-angle scattering clearly plays a crucial role in determining the spatial distribution of the precipitating electron energy flux.

[44] Comparisons of the simulated storm time energy flux under strong diffusion (model 1) with average NOAA-12 precipitating electron energy flux reveals that the simulated storm time energy flux with strong diffusion tends to be much more intense in the evening sector and much weaker near dawn than what is statistically observed. Our simulations show that the most intense electron precipitation under strong diffusion will occur where the electron drift times from the plasma sheet are on the order of the electron lifetime against strong diffusion. On the other hand, comparisons of simulated distributions of the precipitating electron energy flux with a postulated MLT-dependent diffusion that is less than everywhere strong (model 2) with the average NOAA-12 data and Polar/UVI images shows that that this scattering model produces a more realistic diffuse aurora than with strong diffusion (model 1). Comparisons of simulated distributions of the X-ray flux with those obtained by Polar/PIXIE images also show better agreement with scattering model 2 rather than model 1. Our numerical experiment strongly suggests that wave scattering is weak in the post dusk sector (minimum at 2200 MLT) and strong in the morning sector (maximum at 0400 MLT). Both storm time (J. Roeder, private communication, 2004) and statistical [*Koons and Roeder*, 1990] analyses of SCATHA wave data indicate that the observed wave activity is indeed strongest in the morning sector and weakest in the post dusk sector. With scattering model 2, the precipitating electron energy flux and X-ray intensity tends to be higher in the morning sector than in the evening sector because the lifetimes against pitch-angle scattering tend to be shorter in the morning sector than in the evening sector.

[45] The fairly good agreement between our simulation results and the observations are encouraging. However, the MLT-dependent scattering model presented here is only an approximation of what is actually occurring. Certainly the pitch-angle scattering depends not only on MLAT and MLT but also is time dependent. We plan to improve upon our scattering rate models as more relevant wave and particle observations are analyzed. For example, *Horne and Thorne* [2000] have recently calculated pitch-angle diffusion rates for electron cyclotron harmonic (ECH) and whistler mode waves in the equatorial region by using parameters that are representative of CRRES wave observations of *Meredith et al.* [1999]. We will further improve upon our scattering rate model by incorporating results from similar future calculations (e.g., R. M. Thorne, personal communication, 2003) of pitch angle diffusion rates for a wider range of plasma parameters and L values. Recent statistical and storm time analyses of amplitudes of ECH and whistler mode chorus observed by SCATHA (J. Roeder, private communication, 2004) will also aid us in this endeavor.

[46] **Acknowledgments.** The authors thank D. L. McKenzie for providing the PIXIE X-ray production efficiency curve shown in Figure 8. The authors are grateful to M. Thomsen who provided the geosynchronous LANL/MPA satellite data. The authors thank R. M. Thorne for useful discussions on electron lifetimes in the plasma sheet and J. L. Roeder for helpful explanations of SCATHA wave data. The work of M. W. Chen was supported by NASA grant NAG5-12048 and NSF grant NSF-ATM-0202108. The work of M. W. Chen was also supported under The Aerospace Corporation's Independent Research and Development Program. The work of M. Schulz was supported by NASA contract NAS5-30372, by NSF grant ATM-0000340, and by the Independent Research and Development Program of Lockheed Martin Space Systems Company. The work of P. C. Anderson was supported by NASA grant NAG5-11696. The work of G. A. Germany was supported by NASA UVI funding from University of California, Berkeley, subaward SA3527 to the University of Alabama in Huntsville and by NASA grant NAG5-10743. The work of M. Wüest was supported in part by NSF grant ATM9819915. Computing resources were provided by the Maui High Performance Computing Center. The *Dst* indices was downloaded from the World Data Center of Geomagnetism, Kyoto website. The IMF data were downloaded from CDAWeb.

[47] Shadia Rifai Habbal thanks C.-I. Meng and another referee for their assistance in evaluating this paper.

References

Abel, B., and R. M. Thorne (1998), Electron scattering loss in Earth's inner magnetosphere: 1. Dominant physical processes, *J. Geophys. Res.*, 2385–2396.

Albert, J. M. (1994), Quasi-linear pitch angle diffusion coefficients: Retaining high harmonics, *J. Geophys. Res.*, *99*, 23,741–23,745.

Anderson, P. C., D. L. McKenzie, M. J. Brittnacher, M. W. Chen, M. Hairston, and M. F. Thomsen (2000a), Global storm time auroral X-ray morphology and timing and comparison with UV measurements, *J. Geophys. Res.*, *105*, 15,757–15,777.

Anderson, P. C., D. L. McKenzie, L. R. Lyons, and M. Hairston (2000b), Global x-ray observations of magnetospheric convection-driven auroral disturbances, *Geophys. Res. Lett.*, *20*, 3233–3236.

Anderson, P. C., D. L. Carpenter, K. Tsuruda, T. Mukai, and F. J. Rich (2001), Multi-satellite observations of rapid subauroral ion drifts (SAID), *J. Geophys. Res.*, *106*, 29,585–29,600.

Ashour-Abdalla, M., and C. F. Kennel (1978), Diffuse auroral precipitation, *J. Geomagn. Geolectr.*, *30*, 239–255.

Bame, S. J., D. J. McComas, M. F. Thomsen, B. L. Barraclough, R. C. Elphic, J. P. Glore, J. T. Gosling, J. C. Chavez, E. P. Evans, and F. J. Wymer (1993), Magnetospheric plasma analyzer for spacecraft with constrained resources, *Rev. Sci. Instrum.*, *64*(4), 1026–1033.

Belmont, G., D. Fontaine, and P. Canu (1983), Are equatorial electron cyclotron waves responsible for diffuse auroral electron precipitation?, *J. Geophys. Res.*, *88*, 9163–9170.

Boonsiriseth, A., R. M. Thorne, G. Lu, V. K. Jordanova, M. F. Thomsen, and D. M. Ober (2001), A semi-empirical equatorial mapping of AMIE convection electric potentials (MACEP) for the January 10, 1997 magnetic storm, *J. Geophys. Res.*, *106*, 12,903–12,918.

Brice, N. M. (1967), Bulk motion of the magnetosphere, *J. Geophys. Res.*, *72*, 5193–5211.

Chen, M. W., and M. Schulz (2001a), Simulations of storm time diffuse aurora with plasmasheet electrons in strong pitch angle diffusion, *J. Geophys. Res.*, *106*, 1873–1886.

Chen, M. W., and M. Schulz (2001b), Simulations of diffuse aurora with plasma sheet electrons in pitch angle diffusion less than everywhere strong, *J. Geophys. Res.*, *106*, 28,966–28,966.

Chen, M. W., M. Schulz, J. L. Roeder, J. F. Fennell, and L. R. Lyons (1998), Simulations of ring current proton pitch angle distributions, *J. Geophys. Res.*, *103*, 165–178.

Chen, M. W., M. Schulz, G. Lu, and L. R. Lyons (2003), Quasi-steady drift paths in a model magnetosphere with AMIE electric field: Implications for ring current formation, *J. Geophys. Res.*, *108*(A5), 1180, doi:10.1029/2002JA009584.

Cornilleau-Wehrlin, N., J. Solomon, A. Korth, and G. Kremser (1985), Experimental study of the relationship between energetic electrons and ELF waves observed on board GEOS: A support to quasi-linear theory, *J. Geophys. Res.*, *90*, 4141.

Dungey, J. W. (1963), The structure of the exosphere or adventures in velocity space, in *Geophysics, The Earth's Environment*, edited by C. DeWitt, J. Hieblot, and A. Lebeau, pp. 503–550, Gordon and Breach, London.

Fairfield, D. H., and A. F. Viñas (1984), The inner edge of the plasma sheet and the diffuse aurora, *J. Geophys. Res.*, *89*, 841–854.
Fontaine, D., and M. Blanc (1983), A theoretical approach to the morphology and the dynamics of diffuse auroral zones, *J. Geophys. Res.*, *88*, 7171–7184.
Gough, M. P., P. J. Christiansen, G. Martelli, and E. J. Gershuny (1979), Interaction of electrostatic waves with warm electrons at the geomagnetic equator, *Nature*, *279*, 515.
Harel, M., R. A. Wolf, P. H. Reiff, R. W. Spiro, W. J. Burke, F. J. Rich, and M. Smiddy (1981), Quantitative simulation of a magnetospheric substorm: 1. Model logic and overview, *J. Geophys. Res.*, *86*, 2217–2241.
Horne, R. B., and R. M. Thorne (2000), Electron pitch angle diffusion by electrostatic electron cyclotron harmonic waves: The origin of pancake distributions, *J. Geophys. Res.*, *105*, 5391–5402.
Horne, R. B., R. M. Thorne, N. P. Meredith, and R. R. Anderson (2003), Diffuse auroral electron scattering by electron cyclotron harmonic and whistler mode waves during an isolated substorm, *J. Geophys. Res.*, *108*(A7), 1290, doi:10.1029/2002JA009736.
Imhof, W. L., et al. (1995), The Polar Ionospheric X-ray Imaging Experiment (PIXIE), *Space Sci. Rev.*, *71*, 385.
Johnstone, A. D. (1996), Pitch angle diffusion of low energy electrons and positive ions in the inner magnetosphere: A review of observations and theory, *Adv. Space Res.*, *17*, 1089–1098.
Johnstone, A. D., D. M. Walton, R. Liu, and D. A. Hardy (1993), Pitch angle diffusion of low-energy electrons by whistler mode waves, *J. Geophys. Res.*, *98*, 5959–5967.
Kennel, C. F., and M. Ashour-Abdalla (1982), Electrostatic waves and the strong diffusion of magnetospheric electrons, in *Magnetospheric Plasma Physics*, edited by A. Nishida, pp. 245–344, Cent. for Acad. Publ., Tokyo.
Kennel, C. F., F. L. Scarf, R. W. Fredricks, J. H. McGehee, and F. V. Coroniti (1970), VLF electric field observations in the magnetosphere, *J. Geophys. Res.*, *75*, 6136–6152.
Koons, H. C., and J. L. Roeder (1990), A survey of equatorial magnetospheric wave activity between 5 and 8 R_E, *Planet. Space Sci.*, *38*, 1335–1341.
Lyons, L. R., and R. M. Thorne (1973), Equilibrium structure of radiation belt electrons, *J. Geophys. Res.*, *78*, 2142–2149.
McComas, D. J., S. J. Bame, B. L. Barraclough, J. R. Donart, R. C. Elphic, J. T. Gosling, M. B. Moldwin, K. R. Moore, and M. F. Thomsen (1993), Magnetospheric plasma analyzer: Initial three-spacecraft observations from geosynchronous orbit, *J. Geophys. Res.*, *98*, 13,453–13,466.
Meredith, N. P., A. D. Johnstone, S. Szita, R. B. Horne, and R. R. Anderson (1999), "Pancake" electron distributions in the outer radiation belts, *J. Geophys. Res.*, *104*, 12,431–12,444.
Meredith, N. P., R. B. Horne, A. D. Johnstone, and R. R. Anderson (2000), The temporal evolution of electron distributions and associated wave activity following substorm injections in the inner magnetosphere, *J. Geophys. Res.*, *105*, 12,907–12,917.
Nishida, A. (1966), Formation of the plasmapause, or magnetospheric plasma knee, by the combined action of magnetospheric convection and plasma escape from the tail, *J. Geophys. Res.*, *71*, 5669–5679.
Press, W. H., B. P. Flannery, S. A. Teukolsky, and W. T. Vettering (1986), *Numerical Recipes*, Cambridge Univ. Press, New York.
Raben, V. J., D. S. Evans, H. H. Sauer, S. R. Sahm, and M. Huynh (1995), TIROS/NOAA satellite space environment monitor data archive documentation: 1995 update, *Tech. Memo. ERL SEL-86*, Natl. Ocean. and Atmos. Admin., Silver Spring, Md.
Richmond, A. D., and Y. Kamide (1988), Mapping electrodynamic features of the high-latitude ionosphere from localized observations: Technique, *J. Geophys. Res.*, *93*, 5471–5759.
Roberts, C. S. (1969), Pitch-angle diffusion of electrons in the magnetosphere, *Rev. Geophys.*, *7*, 305–337.
Roeder, J. L., and H. C. Koons (1989), A survey of electron cyclotron waves in the magnetosphere and the diffuse auroral electron precipitation, *J. Geophys. Res.*, *94*, 2529–2541.
Rosenbluth, M. N., and C. L. Longmire (1957), Stability of plasmas confined by magnetic fields, *Ann. Physics*, *1*, 120–140.
Rowland, D. E., and J. R. Wygant (1998), Dependence of the large-scale, inner magnetospheric electric field on geomagnetic activity, *J. Geophys. Res.*, *103*, 14,959–14,964.
Scarf, F. L., R. W. Fredricks, C. F. Kennel, and F. V. Coroniti (1973), Satellite studies of magnetospheric substorms on August 15, 1968: OGO 5 plasma wave observations, *J. Geophys. Res.*, *78*, 3119.
Schulz, M. (1974a), Particle lifetimes in strong diffusion, *Astrophys. Space Sci.*, *31*, 37–42.
Schulz, M. (1979b), Particle saturation of the outer zone: A nonlinear model, *Astrophys. Space Sci.*, *29*, 233–242.
Schulz, M. (1991), The magnetosphere, in *Geomagnetism*, edited by J. A. Jacobs, pp. 87–293, Elsevier, New York.
Schulz, M. (1998), Particle drift and loss rates under strong pitch angle diffusion in Dungey's model magnetosphere, *J. Geophys. Res.*, *103*, 61–67.
Schulz, M., and M. W. Chen (1999), Phase-space density mappings of diffuse auroral electrons under strong pitch-angle diffusion in Dungey's model magnetosphere, *Adv. Space Res.*, *23*(10), 1739–1746.
Schumaker, T. L., M. S. Gussenhoven, D. A. Hardy, and R. L. Carovillano (1989), The relationship between diffuse auroral and plasma sheet electron distributions near local midnight, *J. Geophys. Res.*, *94*, 10,061–10,078.
Southwood, D. J. (1977), The role of hot plasma in magnetospheric convection, *J. Geophys. Res.*, *82*, 5512–5520.
Stern, D. (1974), Models of the Earth's electric field, *Rep. X-602-74-159*, NASA Goddard Space Flight Cent., Greenbelt, Md.
Stern, D. P. (1975), Quantitative models of magnetic and electric fields in the magnetosphere, *Rep. X-602-75-90*, NASA Goddard Space Flight Cent., Greenbelt, Md.
Stiles, G. S., E. W. Hones Jr., S. J. Bame, and J. R. Asbridge (1978), Plasma sheet pressure anisotropies, *J. Geophys. Res.*, *83*, 3166–3172.
Torr, M. R., et al. (1995), A far ultraviolet imager for the International Solar-Terrestrial Physics mission, *Space Sci. Rev.*, *71*, 329.
Tsyganenko, N. A. (1989), Magnetospheric magnetic field model with a warped tail current sheet, *Planet Space Sci.*, *37*, 5.
Van Allen, J. A. (1969), Charged particles in the magnetosphere, *Rev. Geophys.*, *7*, 233–255.
Villalón, E., and W. J. Burke (1995), Pitch angle scattering of diffuse auroral electrons by whistler mode waves, *J. Geophys. Res.*, *100*, 19,361–19,369.
Volland, H. (1973), A semiempirical model of large-scale magnetospheric electric fields, *J. Geophys. Res.*, *78*, 171–180.
Volland, H. (1975), Models of global electric fields within the magnetosphere, *Ann. Geophys.*, *31*, 154–173.
Walt, M. (1964), The effects of atmospheric collisions on geomagnetically trapped electrons, *J. Geophys. Res.*, *69*, 3947–3958.
Wolf, R. A., M. Harel, R. W. Spiro, G.-H. Voight, P. H. Reiff, and C.-K. Chen (1982), Computer simulation of inner magnetospheric dynamics for the magnetic storm of July 29, 1977, *J. Geophys. Res.*, *87*, 5949–5962.
Wüest, M., R. A. Frahm, K. Jennings, and J. R. Sharber (2005), Forecasting electron precipitation based on predicted geomagnetic activity, *Adv. Space Res.*, in press.
Wygant, J., D. Rowland, H. Singer, M. Temerin, and M. K. Hudson (1998), Experimental evidence on the role of the large spatial scale electric field in creating the ring current, *J. Geophys. Res.*, *103*, 29,527–29,544.
Yeh, H.-C., J. C. Foster, F. J. Rich, and W. Swider (1991), Storm time electric field penetration observed at mid-latitude, *J. Geophys. Res.*, *96*, 5707–5721.

P. C. Anderson, University of Dallas at Texas, Box 830688, FO22, Richardson, TX 75083, USA.
M. W. Chen, Space Sciences Applications Laboratory, The Aerospace Corporation, P. O. Box 92957, M2-260, Los Angeles, CA 90009-2957, USA. (margaret.w.chen@aero.org)
G. Germany, University of Alabama, 5131 Technology Hall, Huntsville, AL 35899, USA.
G. Lu, High Altitude Observatory, 3450 Mitchell Lane, Boulder, CO 80307-3000, USA.
M. Schulz, Lockheed Martin Advanced Technology Center, 3251 Hanover Street, O/H1-11, Palo Alto, CA 94304, USA.
M. Wüest, Inficon AG, Alte Landstrasse 6, FL-9496 Balzers, Liechtenstein.